**Title:** Preoptic Neurons that Regulate Hibernation Entry

**Authors:** Adrian J. Martinez[1,2]†, Christopher M. Reid[1]†, Aurora J. Lavin-Peter[1], Wenhui Li[1], Andrew S. Lee[1], Eric C. Griffith[3], Sinisa Hrvatin[1,4,5*]

**Affiliations:**

[1]Whitehead Institute for Biomedical Research, Cambridge, MA 02142, USA

[2]Department of Brain and Cognitive Sciences, Massachusetts Institute of Technology, Cambridge, MA 02142, USA

[3]Department of Neurobiology, Harvard Medical School, Boston, MA 02115, USA

[4]Department of Biology, Massachusetts Institute of Technology, Cambridge, MA 02142, USA

[5]Howard Hughes Medical Institute, Massachusetts Institute of Technology, Cambridge, MA, USA

*Corresponding author. Email shrvatin@wi.mit.edu (S.H.)

† These authors contributed equally to this work

**Abstract:** Seasonal hibernation allows species to survive harsh environments by entering a profound hypometabolic and hypothermic state called deep torpor (DT). However, the neural mechanisms controlling entry into this state remain poorly understood. Here, we map neuronal activity across hibernation stages in the Syrian hamster and identify DT-associated activity in the hypothalamic anterior preoptic area (aPOA) as essential for hibernation entry. Single-nucleus multiomic profiling enabled the design of a novel enhancer adeno-associated virus selectively targeting candidate glutamatergic neuronal subpopulations. Using this tool, we demonstrate that activity of a subpopulation of *Samd3*-positive glutamatergic neurons in the hamster aPOA is both necessary and sufficient for DT induction. Together, our findings identify a neuronal population regulating hibernation entry and provide the first genetic access to manipulate this complex behavior.

**Main Text:** The ability to maintain body temperature ($T_b$) within a narrow range is a defining feature of homeotherm physiology[1,2]. However, to survive extreme environmental conditions, many mammals can initiate hypothermic and hypometabolic energy-conserving strategies such as hibernation or daily torpor[3–8]. While $T_b$, heart rate, and metabolic rate decreases observed in daily torpor last only several hours[9,10], seasonal hibernation is characterized by deeper, repeated multi-day bouts of torpor periodically interrupted by arousals to euthermic $T_b$[5,11–15]. Decades of study have characterized the homeostatic thermoregulatory circuitry that detects and responds to internal and external thermal cues[1,2,16–27]. However, despite evidence that ambient and internal temperature[3], circadian clocks[28,29], adenosine, melatonin, and thyroid hormone signaling[30–39], and the peripheral nervous system[40] modulate hibernation dynamics, the neural mechanisms that initiate and sustain deep torpor (DT) in hibernating animals remain largely unexplored.

To probe the neural mechanisms that control entry into hibernation-associated deep torpor, we established a laboratory paradigm of hibernation in the Syrian hamster (*Mesocricetus auratus*), implanting each animal with telemetric temperature probes for continuous $T_b$ monitoring. To induce hibernation, adult (5-6-week-old) animals housed at room temperature (~22ºC) with standard photoperiod (12 hours light (L): 12 hours dark (D)) were first shifted to a short photoperiod (8L:16D) for 8-10 weeks, followed by transfer to 4-5°C ambient temperature conditions to simulate seasonal changes (Fig. 1a, b, Extended Data Fig. 1a). While this paradigm induced hibernation in both males and females, female hamsters were initially found to hibernate more readily (data not shown), with ~80% initiating torpor bouts within six weeks of ambient temperature reduction. As a result, we restricted our subsequent analyses to females.

52 While typical torpor-associated $T_b$ decreases followed an exponential decay curve (n
53 = 1262 torpor bouts, Extended Data Fig. 1b), animals exhibited some variability in torpor
54 dynamics. Altogether, 69% of animals (n = 271) achieved DT (minimal $T_b$ = 5.5 ± 0.5°C,
55 bout duration 60.3 ± 13.4 h) and 11% (n = 42) exhibited only shallow torpor bouts (minimal
56 $T_b$ = 12.2 ± 3.1°C, bout duration 6.8 ± 1.8 h), with 20% (n = 81) failing to initiate torpor
57 during the 6-week observation period (Fig. 1c-f, Extended Data Fig. 1c). Periods of
58 interbout euthermia (IBE) between DT bouts lasted 15.3 ± 2.8 h (n = 2471 IBE periods,
59 Fig. 1e). Moreover, consistent with prior reports[41], torpor entry occurred preferentially
60 during subjective night (~ZT17-18) (n = 3,595 torpor bouts, Fig. 1g) and was
61 characterized by a stereotyped nesting behavior with curled posture and absence of gross
62 motor movement, food, or water intake[5,15]. By contrast, arousal from DT exhibited no clear
63 circadian pattern (Fig. 1h), consonant with disrupted circadian clock oscillations at
64 temperatures below 15°C[41,42].

65

66 **POA activity regulates hamster entry into deep torpor**

67 Having established laboratory conditions for efficient hibernation induction, we
68 employed this system to investigate neural activity changes associated with DT onset. To
69 this end, we collected brain samples during DT and IBE, as well as from non-hibernating
70 control animals, and performed immunostaining for FOS, a marker of neuronal activity
71 (Fig. 2a). Given prior reports of neuronal activity marker induction in hypothalamic regions
72 during DT bouts[41,43,44], and classic studies showing that hypothalamic lesions disrupt $T_b$
73 regulation during hibernation[45], we focused our analysis primarily on the hypothalamus.
74 Among the 32 distinct regions analyzed, we observed DT-active regions associated with

75 circadian rhythm modulation (Suprachiasmatic nucleus)[46–48], energy homeostasis
76 (Arcuate nucleus)[49–51], and arousal (Paraventricular nucleus of the thalamus)[52,53].
77 Notably, the anteroventral periventricular nucleus (AVPe) within the anterior POA
78 exhibited the highest degree of FOS induction in DT relative to IBE or non-hibernating
79 control samples (14.1% vs. 6.9% and 0.8%, $P = 0.0685$ and $P < 0.001$, respectively) (Fig.
80 2b-d, Supplementary Tables 1, 2, Extended Data Fig. 2a, b).

81 To test directly whether hypothalamic neuronal activity is required for the initiation and
82 maintenance of hibernation, we stereotaxically injected adeno-associated virus (AAV)
83 expressing an inhibitory Gi-coupled DREADD (Designer Receptor Exclusively Activated
84 by Designer Drug; AAV-hSyn-hM4D(Gi)-mCherry)[54] into hibernating hamsters (Fig. 2e),
85 systematically targeting different areas of the anterior hypothalamus that exhibited
86 substantial DT-associated activity. After allowing animals to recover and resume DT
87 bouts, we administered the DREADD agonist clozapine (CLZ) via drinking water. As
88 animals consumed CLZ during their IBE periods, we observed a cessation of torpor bouts
89 in a subset (4/13) of the tested animals, while all animals that underwent sham surgery
90 and received CLZ (5/5) readily re-entered torpor (Fig. 2f-h, Extended Data Fig. 2c).
91 Correlation of the pattern of Gi-DREADD expression across animals with the degree of
92 DT perturbation identified subregions of the anterior POA (aPOA), including the medial
93 preoptic area (MPO), medial preoptic nucleus (MPN), and AVPe, as regions whose
94 silencing was associated with perturbed hibernation (Fig. 2h-j, Supplementary Table 3).
95 Together, these findings implicate the anterior preoptic area as a key region whose
96 activity is necessary for the initiation of DT bouts during hibernation.

97

98 **Cross-species transcriptomic profiling identifies DT-active neuronal populations**

99 The aPOA has been implicated in the regulation of fasting-induced daily torpor (FIT)
100 in mice[43,55–59]. Our chemogenetic silencing studies in hamster therefore raised the
101 possibility that this region plays a conserved role in the control of hypometabolic states
102 across mammals. To gain further insight into the diversity of neural cell types in the
103 hamster POA and their relation to the cellular composition of the murine POA, we
104 dissected and profiled the POA of 7 adult hamsters (4 females and 3 males) using single-
105 nucleus paired RNA- and ATAC- sequencing (multiome) (Fig. 3a). We annotated the
106 hamster POA cells by aligning and integrating the resulting data with recently published
107 mouse POA multiome and spatial transcriptomic datasets[60,61], generating the first
108 multiomic cross-species POA cellular taxonomy (Extended Data Fig. 3-5).

109 Since activity of brain regions within the median and medial POA was essential for DT
110 entry (Fig. 2i), we focused our analysis on these regions. Graph-based clustering
111 identified major neuronal and non-neuronal cell classes, with further subclustering of
112 neuronal cells (*n* = 26,761 cells) identifying 15 distinct GABAergic and 11 glutamatergic
113 neuronal cell types shared between hamster and mouse (Fig. 3b-d, Extended Data
114 Fig. 4). Importantly, every neuronal cluster contained both mouse and hamster cells (Fig.
115 3c), and pair-wise transcriptional similarity analysis (cosine similarity score) between all
116 hamster and murine neuronal cell clusters revealed consistent 1:1 cross-species
117 relationships, further supporting the validity of our cross-species atlas alignment (Fig. 3e).
118 Moreover, with the exception of a few cell types, the relative cell type abundance across
119 POA neuronal clusters was largely preserved between hamster and mouse (Extended

120 Data Fig. 5e). Thus, our analyses reveal broad cellular homology between hamster and
121 mouse POA.

122 Focusing more closely on POA neuronal populations implicated in FIT in the mouse,
123 we found that the expression patterns of molecular markers of mouse FIT-associated
124 neurons (*Slc17a6/Vglut2, Adcyap1, Esr1,* and *Ptger3*) were broadly conserved across
125 hamster and mouse POA cell types (Fig. 3f, g). Moreover, *in situ* hybridization (ISH)
126 analysis indicated that *Vglut2* and *Adcyap1*, two broad markers of FIT-regulating cells,
127 labeled neurons in similar anatomical locations in the mouse and hamster aPOA,
128 including the AVPe, MPO, and MnPO (animals = 4, Fig. 3h, Extended Data Fig. 6).
129 Leveraging these findings, we carried out combined immunostaining and ISH on aPOA
130 samples from hamsters (n = 3) in deep torpor and found that the majority of DT-active
131 (FOS-positive) neurons express *Slc17a6/Vglut2* (65.2 ± 4.2%, animals = 3), with a
132 considerable portion expressing *Adcyap1* (34.0 ± 1.4%, animals = 3), and relatively few
133 expressing *Slc32a1/Vgat* (12.8 ± 1.5%, animals = 3, Fig. 3i, j, Extended Data Fig. 7a, b).
134 Together, these findings suggest that homologous aPOA glutamatergic neuronal
135 populations may be active during mouse FIT and hamster DT.

136 To further test this idea, we leveraged anatomical information from our transcriptomic
137 and anatomical atlas to identify Glut-04, -06, -07, -09, -10, and -11 clusters as
138 corresponding to FIT-regulating neurons (hereafter collectively termed $aPOA^{Vglut2}$
139 neurons; Fig. 3k, Extended Data Fig. 7c), and expression of the *Samd3* gene was found
140 to exclusively mark this population (Fig. 3l). Indeed, a substantial fraction of hamster DT-
141 active (FOS+) neurons also expressed *Samd3* (46.4 ± 4.1% of FOS+ AVPe neurons are
142 positive for *Samd3* mRNA, Fig. 3m, n), further supporting the idea that $aPOA^{Vglut2}$ neurons

143 are active during DT entry and might regulate entry into this state. Together, our findings
144 establish the first cross-species atlas of the aPOA, a key region whose activity is
145 necessary for the initiation of DT bouts during hibernation, uncovering broad homology
146 between mouse and hamster cell types and implicating aPOA$^{Vglut2}$ neurons as promising
147 candidate drivers of DT entry in the hamster.

148

149 **Enhancer-driven viral tools to access aPOA$^{Vglut2}$ neurons**

150 To assess the functional role of aPOA$^{Vglut2}$ neurons in hamster DT entry, we required
151 the ability to selectively target and manipulate these cell populations *in vivo*. Transgenic
152 options in the hamster remain limited, and a *CamkIIa* promoter-driven AAV exhibits poor
153 specificity for glutamatergic neurons in the hamster POA (42.6 ± 2.0%, animals = 4,
154 Extended Data Fig. 8). Recently, AAV constructs incorporating compact cell-type-specific
155 enhancer gene regulatory elements (GREs) have offered a promising alternative to
156 traditional transgenic technologies in nonstandard species[62–68]. We therefore sought to
157 generate new enhancer-AAV tools driving restricted payload expression in the target
158 aPOA$^{Vglut2}$ cell population.

159 To develop a viral approach to selectively target aPOA$^{Vglut2}$ neurons, we leveraged the
160 extensive murine single-nucleus chromatin accessibility (snATAC-seq) data included in
161 our multiomic cross-species atlas to identify conserved genomic elements exhibiting
162 selectively enhanced accessibility in aPOA$^{Vglut2}$ neuron cell populations (Fig. 4a). First,
163 we employed a modeling-based approach to identify cell-type-specific nucleosome-
164 depleted gene regulatory regions. Subsequently, we performed differential accessibility
165 analysis to identify putative GREs with enriched accessibility in aPOA$^{Vglut2}$ neuronal

166 populations relative to other neuronal subtypes (Fig. 4b, Extended Data Fig. 9), and
167 filtered GREs based on proximity to aPOA$^{Vglut2}$ neuron-restricted marker genes (Fig. 4c).
168 Notably, using this approach, we identified a conserved 500 bp element proximal to the
169 mouse *Samd3* gene, hereafter termed *Samd3E*, that exhibited the highest accessibility
170 enrichment in aPOA$^{Vglut2}$ neurons relative to caudal POA$^{Vglut2}$ neurons and POA$^{Vgat}$
171 neurons (FDR < $10^{-300}$, $\log_2$Fold Enrichment = 3.1, Fig. 4b-e), with similar aPOA$^{Vglut2}$
172 neuron-enriched accessibility also observed in the hamster (P = $10^{-173}$, $\log_2$Fold
173 Enrichment versus other populations = 3.2, Fig. 4f, Extended Data Fig. 9).

174 The resulting candidate mouse GRE sequences were synthesized and cloned into an
175 AAV backbone upstream of a minimal beta-globin promoter sequence and a red
176 fluorescent protein (RFP) reporter transgene prior to packaging into functional AAV8
177 particles for *in vivo* evaluation. Notably, the *Samd3E* element conferred remarkable
178 specificity, restricting reporter expression almost exclusively to *Vglut2*+ neurons in the
179 hamster aPOA (95.2 ± 1.2%; animals = 3), with substantial co-labeling of *Samd3*+ cells
180 (58.7 ± 3.2%, animals = 3, Fig. 4g, h, Extended Data Fig. 10). Taken together, these
181 findings highlight the power of this approach to generate viral tools to study brain circuits
182 across species, including in hibernating animals, and establish the *Samd3E*-driven AAV
183 (Samd3E-AAV) as an effective tool for achieving targeted genetic access to glutamatergic
184 neurons of the anterior POA.

185

186 **aPOA$^{Vglut2}$ neuronal activity is necessary and sufficient for deep torpor entry**

187 Employing our newly developed Samd3E-AAV, we set out to address the role of
188 aPOA$^{Vglut2}$ neuronal activity in hibernation and DT by expressing an inhibitory Gi-

189 DREADD (AAV-Samd3E-hM4D(Gi)-EGFP) in hamster aPOA$^{Vglut2}$ neurons (Fig. 5a).
190 Neuronal inhibition via CLZ administration had no significant effect on basal homeostatic
191 $T_b$ or circadian $T_b$ rhythmicity in control non-hibernating Gi-DREADD-expressing
192 hamsters (Extended Data Fig. 11a, b). However, actively hibernating Gi-DREADD-
193 expressing (n = 12) animals showed a significant delay in the resumption of DT bouts
194 following CLZ treatment compared to when these same animals were administered a
195 water-only vehicle control (114.9 ± 45.4 hours vs. 64.1 ± 24.5 hours, P = 0.0003). Indeed,
196 a majority (7/12) of CLZ-treated Gi-DREADD-expressing animals failed to re-enter DT
197 during the full 6-day course of CLZ treatment, whereas none (0/12) of the animals failed
198 to resume DT during treatment with the vehicle control. Moreover, animals (n = 5)
199 expressing a control reporter payload (AAV-Samd3E-EGFP-Synaptophysin-mRuby)
200 exhibited no significant difference in the time to DT resumption following CLZ or vehicle
201 treatment (61.6 ± 26.5 hours vs. 47.4 ± 10.2 hours, respectively. P = 0.6167), with all
202 animals resuming torpor bouts within the CLZ treatment window (Fig. 5b, c). Together,
203 these results strongly suggest that aPOA$^{Vglut2}$ neuronal activity is required for entry into
204 hibernation-associated DT.

205 To determine the extent to which aPOA$^{Vglut2}$ neuron activity is sufficient to drive DT
206 entry, we selectively introduced an excitatory Gq-DREADD into hamster aPOA$^{Vglut2}$
207 neurons via our Samd3E-AAV (AAV-Samd3E-hM3D(Gq)-EGFP, Fig. 5d). CLZ
208 administration led to a rapid, significant drop in $T_b$ in Gq-DREADD-expressing hamsters,
209 with the animals reaching a minimum body temperature of 13.9 ± 1.0ºC (P < 0.0001
210 relative to normothermia) and maintaining a reduced body temperature for 56.9 ± 13.1
211 hours, consistent with the induction of a prolonged torpor-like state (Fig. 5e-g). By

212 contrast, these same animals exhibited no discernable $T_b$ change upon control PBS
213 administration (minimal $T_b$ = 33.3 ± 2.4ºC, P = 0.8959 relative to normothermia). In
214 addition, CLZ treatment of Gq-DREADD-expressing animals (n = 6), but not PBS
215 treatment of the same animals (n = 6) or PBS/CLZ treatment of hamsters injected with a
216 control viral construct (n = 3), induced behaviors consonant with torpor entry, including a
217 curled posture and prolonged inactivity in the nest (P = 0.0168, Fig. 5h, i, Extended Data
218 Fig. 12, Supplementary Video 1). Moreover, follow-up analyses revealed that the depth
219 of CLZ-induced torpor across animals correlated with levels of aPOA Gq-DREADD
220 expression, suggesting that more extensive $aPOA^{Vglut2}$ neuron activation drives deeper
221 torpor-like bouts (r = -0.9577, P = 0.0104, Extended Data Fig. 11c, d). Together, these
222 findings show that $aPOA^{Vglut2}$ neuronal activity is both necessary and sufficient to initiate
223 a profound $T_b$ decrease and DT-associated nesting behaviors in the hamster.

224 Finally, given that $aPOA^{Vglut2}$ neurons are present in both the Syrian hamster (a
225 hibernator) and mouse (non-hibernator), we investigated whether virus-mediated
226 chemogenetic activation of this neuronal population in mice housed at low ambient
227 temperatures would drive a DT-like decrease in $T_b$. Indeed, CLZ treatment of Samd3E-
228 Gq-DREADD-transduced mice yielded a rapid and sustained drop in body temperature,
229 although markedly less than that observed in hamsters (Extended Data Fig. 13). Thus,
230 $aPOA^{Vglut2}$ neuronal activation is sufficient to elicit acute, pronounced reductions in core
231 temperature in both hibernating and non-hibernating species, with the difference in
232 magnitude suggestive of potential hibernator-specific evolutionary modifications in
233 downstream effector circuitry.

234

235 **Discussion**

236 Hibernation is a conserved, recurrently evolved energy-conserving strategy across
237 the mammalian lineage[5,6]. Entry into this state is orchestrated by a complex interplay of
238 environmental cues and endocrine signals[69]. However, despite prior reports of
239 hibernation-associated neural activity changes and classic lesion studies implicating the
240 POA[41,43–45], the specific neuronal populations regulating entry into hibernation-associated
241 deep torpor remained unknown. Here, using a Syrian hamster model, we combine neural
242 activity mapping with chemogenetic silencing to show that aPOA activity is essential for
243 deep torpor entry.

244 Our single-nucleus transcriptional and epigenomic profiling of the hamster POA
245 revealed strong cellular homology with the mouse, with no evidence of distinct cell
246 populations. Instead, we observed that aPOA glutamatergic neurons homologous to FIT-
247 regulating neuronal cell types in the mouse exhibit elevated activity upon hibernation-
248 associated DT in the hamster. Through the development and use of a novel enhancer-
249 driven AAV we show that aPOA$^{Vglut2}$ neuron silencing blocks hibernation-associated DT
250 entry, whereas chemogenetic activation of this population drives a rapid fall in body
251 temperature and hibernation-like nesting behavior. Together, these studies establish
252 Samd3E-AAV-targeted aPOA$^{Vglut2}$ neurons as key regulators of hibernation and provide
253 the first genetic access to hibernation-regulating circuits. Moreover, this Samd3E-AAV,
254 as well as the broader enhancer-driven viral targeting strategy, should be broadly
255 applicable to target these and related cell populations in other hibernating species.

256 Although mouse FIT and seasonal hibernation both involve profound reductions in $T_b$,
257 metabolic rate, and heart rate, these states differ markedly in their depth, duration, and

258 ethological significance. FIT represents a short-term response to food scarcity, lasting
259 only hours, whereas hibernation is typically a seasonal behavior involving deeper, multi-
260 day torpor bouts punctuated by brief periods of interbout euthermia. Our findings raise
261 the possibility that these differences reflect distinct connectivity and/or activity patterns of
262 aPOA$^{Vglut2}$ neurons in the two species, which might derive in part from remaining cross-
263 species gene expression differences observed in these cell types (Extended Data Fig.
264 7d). Moreover, chemogenetic activation of the aPOA$^{Vglut2}$ neurons in hamsters drives
265 substantially deeper torpor bouts than in mice, which might reflect limited efficiency in
266 fully targeting the aPOA$^{Vglut2}$ neuronal population (Extended Data Fig. 10) or alternatively
267 might indicate a requirement for additional circuit elements for the full expression of deep
268 torpor in the hamster. Similarly, in the future it will be important to determine whether this
269 aPOA$^{Vglut2}$ neuronal population, or aspects of the broader hibernation-regulating circuitry,
270 undergoes active remodeling during the extended pre-hibernation conditioning period to
271 support prolonged bouts of deep torpor.

272 More broadly, our findings in hamster and mouse further support for the idea that
273 regulated heterothermy is an ancestral trait in mammals[70,71] and that core elements of
274 the underlying torpor circuitry may be broadly conserved—potentially not only across
275 torpid and hibernating mammals, but also in species that do not naturally exhibit these
276 states. Indeed, *in situ* hybridization data from the marmoset (*Callithrix jacchus*), a non-
277 hibernating primate, indicate that neurons expressing deep torpor-associated markers
278 are present in the homologous regions within the aPOA (Extended Data Fig. 14)[72–74].
279 Our study thus lays a foundation for future efforts to define broader hibernation-
280 regulating circuitry, including upstream inputs conveying seasonal cues, downstream

281 pathways mediating systemic adaptations, and the cellular mechanisms that allow
282 neurons to function at near-freezing temperatures. Beyond advancing basic
283 understanding of hibernation, these insights may eventually inform approaches to
284 harness the mechanisms behind this amazing adaption to advance medicine in areas
285 such as therapeutic hypothermia, organ preservation, central metabolic control,
286 suppression of muscle atrophy, and aging.

287 **Methods**

288 **Animals**

289 Animal experiments were approved by the Massachusetts Institute of Technology
290 Committee of Animal Care (Protocol 2503000788), following ethical guidelines described
291 in the US National Institutes of Health Guide for the Care and Use of Laboratory Animals
292 and the Animal Welfare Act.

293 **Hamster.** For all experiments, unless otherwise noted, adult female (5-6-week-
294 old) Syrian hamsters (Inotiv, Strain HsdHan:AURA, Stock 089) were used. Hamsters
295 were singly caged and initially housed at 22°C under a standard 12-hour light/dark cycle
296 (12L:12D) cycle in temperature- and humidity-controlled rooms and had *ad libitum* access
297 to food and water.

298 **Mouse.** Adult female (8-week-old) C57BL/6J (JAX #000664) mice were used. All
299 mice were group housed initially at 22°C under a standard 12L:12D cycle in temperature-
300 and humidity-controlled rooms and had *ad libitum* access to food and water.

301 No statistical methods were used to predetermine the sample size. Hamsters were
302 randomly assigned to experimental groups before surgery. Where possible, investigators
303 were blinded during analysis.

304

305 **Hibernation Induction**

306 Utilizing a modified hibernation paradigm[15,75] female (5-6-week-old) hamsters
307 were singly caged and housed at 22°C under a standard 12L:12D cycle for a short period
308 to acclimate to the animal facility. Upon completion of acclimation, hamsters were
309 transferred to a reduced 8L:16D cycle with an ambient temperature of 22°C. After 7-8

310 weeks, hamsters were placed in temperature-controlled chambers with 8L:16D cycle and
311 ambient temperatures of 4-5°C. Initiation of hibernation was confirmed by changes in $T_b$
312 measured by telemetric temperature probes. In all cases, hamsters had *ad libitum* access
313 to food and water.
314
315 **Telemetric monitoring of core body temperature**
316 Within the 7-8-week period of housing at 22°C in 8L:16D cycle, hamsters were
317 anesthetized with 3% isoflurane and implanted with telemetric/logger temperature probes
318 (Star-Oddi, DST microRF-T) in the abdominal cavity. Hamsters were allowed to recover
319 for a minimum of three days before additional procedures or experiments were performed.
320 After recovery and at the end of the 7-8-week period, hamsters were moved to
321 temperature-controlled chambers, and core body temperature was monitored in home
322 cages placed onto a radio frequency receiver antenna (Star-Oddi, Antenna & RF-box).
323 Upon euthanasia, probes were removed and complete logged data downloaded. Core
324 body temperature was logged every 20-30 min.
325
326 **Torpor bout analysis**
327 **Classification.** To classify torpor bouts, we employed a Gaussian Mixture Model
328 in R. The classification was based on minimum body temperature and bout duration. Each
329 bout was assigned to the cluster in which it had the highest posterior probability of
330 membership. A cluster characterized by lower $T_b$ and longer duration was designated as
331 "Deep", whereas the other cluster was classified as "Shallow". Furthermore, periods of
332 between bouts above the set $T_b$ threshold were classified as IBE.

333 **Circadian preference.** In R, circadian preference for torpor and IBE initiation was
334 quantified using the Raleigh test of circular uniformity.
335 **Exponential decay.** In R, elapsed time in torpor for each body temperature
336 reading from torpor bouts classified as deep were determined for the first 30 hours. Next,
337 using the mean of temperatures at each time across animals, a nonlinear model was fit
338 to the data using the minimum temperature within the 30-hour period as a fixed asymptotic
339 value.
340

341 **Viral constructs**

342 AAV8-hSyn-hM4D(Gi)-mCherry (Addgene, 50475-AAV8) was obtained from
343 Addgene. AAV8-Samd3E-dTomato-nlsdTomato, AAV8-Samd3E-hM4D(Gi)-P2A-
344 nlsGFP, AAV8-Samd3E-EGFP-P2A-Synaptophysin-mRuby, and AAV8-Samd3E-
345 hM3D(Gq)-P2A-nlsGFP were produced in-house using the method previously
346 described[76] and titered via digital PCR (QIAGEN, QIAcuity). All viruses were diluted with
347 PBS to a final titer of 1E13 vg/mL before stereotaxic delivery into the hamster brain. For
348 mice, AAV8-Samd3E-hM3D(Gq)-P2A-nlsGFP with a final titer of 5E13 vg/mL was used.
349

350 **Stereotaxic viral injection**

351 **Hamster.** Hamsters were anaesthetized with 3% isoflurane and placed in a
352 stereotaxic head frame (David Kopf Instruments, model 1900). If hamsters were actively
353 hibernating, they were aroused from hibernation and placed at 22°C the day prior to
354 surgery. An air-based injection system connected to a pulled glass needle was used to
355 infuse ~100 nL of virus bilaterally at regions of interest. Hypothalamic regions were

356 targeted by referencing the hamster stereotaxic atlas[77]. When targeting the aPOA,
357 coordinates +1.2 mm AP, ±0.4 mm ML, -7.5mm DV were used. Hamsters were allowed
358 to recover at 22°C for a minimum of 3 days before a return to 4°C chambers. Animals
359 were afforded a recovery period of at least two weeks post-surgery prior to further
360 experimental manipulation to allow for viral expression and, if appropriate, resumption of
361 hibernation.

362 **Mouse.** Mice were anesthetized with 3% isoflurane and placed in a stereotaxic
363 head frame (RWD, Guangdong, China). A Nanoject III (Drummond Scientific, Broomall,
364 PA) system connected to a pulled glass needle was used to infuse ~100 nL of virus
365 bilaterally into the aPOA (distance from Bregma, AP: +0.6 mm, ML: ±0.4 mm, DV: -5.2
366 mm). Mice were monitored for three days post-surgery to ensure full recovery, with a
367 waiting period of at least two weeks to allow sufficient viral expression.

368

369 **Chemogenetic manipulations**

370 **Hamster.** Clozapine dihydrochloride (Hello Bio, HB6129) was either dissolved in
371 sterile water or PBS at a concentration of 10 mg/mL and then stored at -20°C until use.
372 For administration via drinking water, CLZ dissolved in sterile water was diluted in drinking
373 water at a dose of 0.1 mL/kg (1 mg/kg) in a final volume of 250 mL. Animals were
374 maintained on CLZ water for 3-7 days. For intraperitoneal (I.P.) administration, CLZ
375 dissolved in PBS was administered at a dose of 0.5 mL/kg (5 mg/kg). In each case when
376 treating actively hibernating hamsters, they were aroused from hibernation the morning
377 of each experiment and treatment was administered in the evening.

378 **Mouse.** Mice injected with AAV8-Samd3E-hM3D(Gq)-P2A-nlsGFP were single
379 housed and placed in a temperature-controlled chamber at 8°C for three days. After three
380 days, mice were I.P. injected with CLZ at a dose of 5 mg/kg and surface body temperature
381 was measured using a thermal camera (Teledyne FLIR C5, Teledyne Flir, Wilsonville,
382 OR). Images were taken before CLZ injection, and 30 min, 60 min, 3 hours, 6 hours and
383 24 hours after CLZ injection. Analysis of surface body temperature and representative
384 images were generated using the Flir Ignite software (https://ignite.flir.com/).
385
386 **Immunofluorescence**
387 Hamsters were deeply anesthetized with isoflurane and then euthanized by
388 transcardial perfusion of 50 mL ice-cold 1X PBS followed by 50 mL of 4%
389 paraformaldehyde (PFA). Brains were extracted, post-fixed overnight with 4% PFA at
390 4°C, and then embedded in 1X PBS with 3% agarose. Brains were sliced on a vibratome
391 into 50 µm coronal sections and stored at -20°C in cryoprotectant buffer (30% sucrose,
392 1% polyvinyl-pyrrolidone (PVP-40), 30% ethylene glycol, in 0.1 M phosphate buffer).
393 Free-floating coronal sections were washed three times with 1X PBS and then blocked
394 for 1 hour at room temperature with 1X PBS containing 10% donkey serum and 0.3%
395 Triton X-100. Sections were incubated overnight at 4°C with primary antibodies (Rabbit
396 anti-FOS, Synaptic Systems, 226-008; Rabbit anti-RFP, Rockland, 600-401-379; Chicken
397 anti-GFP, Aves Labs, GFP-1020) diluted in 1X PBS containing 5% donkey serum and
398 0.3% Triton X-100, washed again three times with 1X PBS, and incubated for 2 hours at
399 room temperature with secondary antibodies in 1X PBS containing 5% donkey serum and
400 0.3% Triton X-100. After washing three times in 1X PBS, samples were counter-stained

401 for 15 minutes at room temperature with 1 µg/mL DAPI, washed again three times in 1X
402 PBS, and then mounted onto SuperFrost Plus glass slides and coverslipped using
403 Fluoromount-G.
404
405 **Determining deep torpor-active brain regions**
406 Brains were collected in torpor, IBE, and from non-hibernating control animals and
407 were processed as indicated in the section 'Immunofluorescence' using the following
408 reagent for the detection of FOS: Rabbit anti-FOS, Synaptic Systems, 226-008.
409 **Sample imaging.** Sections were imaged with a TissueFAXS SL whole-slide
410 scanning system equipped with a Zeiss Axio Imager Z2 fluorescence microscope and
411 TissueFAXS image acquisition software (Ragon Institute Microscopy Core).
412 **Image analysis**. Using TissueQuest analysis software (TissueGnostics GmbH,
413 Vienna, Austria), brain regions were manually annotated and nuclear DAPI signal
414 segmented. Segmented cells containing putative FOS signal were determined to be FOS-
415 positive based on diameter and mean fluorescence intensity. In R, regional cell counts
416 were analyzed and percent active neurons determined by the fraction of FOS-positive
417 and total DAPI-positive cells. Significance was calculated using a mixed-effects ANOVA
418 with post-hoc pairwise comparisons. Pairwise comparison p-values were multiple tests
419 corrected using the Bonferonni method.
420
421 **Mapping of virally injected hypothalamic nuclei and correlation with**
422 **chemogenetically induced torpor perturbation**

423 Hibernating hamsters were bilaterally injected with AAV8-hSyn-hM4D(Gi)-
424 mCherry. Upon resumption of hibernation, hamsters were administered CLZ water for ~3
425 days (74 hours) to inhibit virally injected regions, and their core body temperature were
426 recorded.

427 **Temperature data analysis.** Upon CLZ water treatment, hamsters reinitiating
428 deep torpor within 48 hours were classified as unperturbed, and those failing to reinitiate
429 (remaining euthermic) within this time were classified as perturbed. Sham surgery control
430 animals treated with CLZ water for 7 days informed this threshold (Extended Data Fig.
431 2c). Absolute elapsed time of euthermia from start of treatment was used for further
432 analysis.

433 **Sample imaging.** Given the unavoidable variability in hypothalamic region
434 targeting and viral spread, all hamsters were euthanized for post hoc assessment of
435 transduced brain regions. Collected brains were processed as indicated in the section
436 'Immunofluorescence' to detect endogenous mCherry fluorescence. Sections were
437 imaged with a TissueFAXS SL whole-slide scanning system equipped with a Zeiss Axio
438 Imager Z2 fluorescence microscope and TissueFAXS image acquisition software (Ragon
439 Institute Microscopy Core).

440 **Image and correlation analysis.** Viral mCherry expression was quantified across
441 70 hypothalamic regions in a semi quantitative manner, where the viral expression was
442 scored 0 (none), 1 (minimal), 2 (partial), or 3 (complete) in each region and hemisphere.
443 The analysis was performed blinded to whether perturbation of torpor was observed in
444 each hamster. To assign a single numeric value for each hypothalamic region in each
445 hamster, we added the semiquantitative expression values from each hemisphere. Next,

446 a Pearson correlation was calculated for each region across all hamsters between the
447 viral expression in that region and the length of time spent euthermic.
448
449 **Nuclei dissociation and single-cell analysis**
450 Preoptic area tissue was dissected from adult male and female Syrian hamsters
451 and immediately flash-frozen. The 10X genomics nuclei isolation kit (1000448) was used
452 to obtain dissociated nuclei. Tissue was homogenized on ice in a detergent-based nuclei
453 isolation buffer, passed through a 40-µm filter, and purified by centrifugation. Nuclei were
454 washed, and counted before loading. Single-nucleus multiome libraries were prepared
455 using the 10x Genomics Chromium Single Cell Multiome ATAC + Gene Expression
456 workflow following the manufacturer's protocol. Constructed libraries were quantified,
457 pooled, and sequenced on an Illumina platform to recommended depth for both
458 modalities. The raw data were processed in parallel with cellranger-arc to generate gene-
459 expression count matrices, ATAC fragment files, and peak-by-cell accessibility matrices.
460 A recently published mouse POA multiome dataset generated with the same 10x system
461 was obtained to build a reference dataset. A combination of scVI and Scanpy[78,79]
462 pipelines were used to process and integrate the two datasets, including quality control
463 (filtering by gene counts, UMI counts, and mitochondrial RNA content), normalization, log-
464 transformation, identification of highly variable genes, dimensionality reduction,
465 neighborhood graph construction, and Leiden clustering.
466 To ensure that downstream analyses focused on POA-associated neuronal
467 populations, we used the MERFISH dataset as a spatial reference[61]. To this end, mouse
468 spatial transcriptomic data was subset to only include neurons found in the mPOA and

469 co-clustered with mouse neuronal snRNA-seq. Canonical POA markers and spatial
470 annotations were used to confirm that the identified clusters in both species corresponded
471 to POA-localized neuronal subtypes. Subsequently, the reference mouse dataset was
472 used to identify homologous hamster neurons through integration and label transferring
473 with scANVI[80]. Chromatin accessibility matrices were analyzed with Pycistopic[81] including
474 psuedobulking, peak calling and filtering, identification of co-accessible regions and
475 differential accessibility analysis.
476
477 **Double fluorescent *in situ* hybridization and immunofluorescence**
478 Hamsters were deeply anesthetized with isoflurane and then euthanized by
479 transcardial perfusion of 50 mL ice-cold 1X PBS followed by 50 mL of 4% PFA. Brains
480 were extracted, post-fixed overnight with 4% PFA at 4°C, and then incubated in 1X PBS
481 with 30% sucrose at 4°C until fully infiltrated and sunk to the bottom of the chamber (72-
482 96 hours). Brains were embedded in Optimal Cutting Temperature (O.C.T.) compound,
483 frozen on dry ice, and stored at -80°C until use. Brains were sliced on a cryostat (Leica
484 CM3050 S) into 10-30 µm coronal sections, placed in cryoprotectant buffer, and stored at
485 −20°C until use. Free-floating coronal sections were washed three times with 1X PBS,
486 mounted onto Superfrost Plus slides, and then baked for 45 minutes at 60°C. Subsequent
487 steps followed the standard fluorescent *in situ* hybridization protocol for the RNAscope
488 Fluorescent Multiplex V2 Assay using the following probes: Mau-*Samd3*-C1 (1826261),
489 Mau-*Slc17a6*-C2 (1176381), Mau-*Adcyap1*-O1-C3 (1808861), Mau-*Slc32a1*-C4
490 (1176381).

491 Upon completion of *in situ* hybridization, samples immediately were processed
492 according to the ACD RNAscope Fluorescent Multiplex V2 Assay Combined with
493 Immunofluorescence manual with the following modifications: Slide-mounted sections
494 were washed twice in 1X TBS with 0.005% Tween-20 (TBST), blocked for 1 hour at room
495 temperature with 1X TBS containing 10% donkey serum, and incubated overnight at 4°C
496 with primary antibodies (Rabbit anti-FOS, Synaptic Systems, 226-008; Rabbit anti-RFP,
497 Rockland, 600-401-379; Chicken anti-GFP, Aves Labs, GFP-1020) diluted in 1X TBS
498 containing 5% donkey serum. Slides were washed three times with TBST, incubated for
499 2 hours at room temperature with secondary antibodies in 1X TBS containing 5% donkey
500 serum, washed again three times with TBST, counter-stained for 15 minutes at room
501 temperature with 1 µg/mL DAPI, washed three times with 1X TBS, and finally mounted
502 on coverslips using ProLong Gold.

503 **Sample imaging.** Sections were either imaged with a TissueFAXS SL whole-slide
504 scanning system equipped with a Zeiss Axio Imager Z2 fluorescence microscope and
505 TissueFAXS image acquisition software (Koch Institute Swanson Biotechnology
506 Center/Microscopy Core) or a Leica Stellaris 8 FALCON confocal microscope (Whitehead
507 Institute W.M. Keck Facility for Biological Imaging).

508 **Image analysis**. Using QuPath software[82], colocalization analysis of RNAscope
509 and immunofluorescent signals was performed. After manual annotation of regions of
510 interest, the InstanSeg extension[83] was utilized for cell segmentation, considering each
511 fluorescent signal. Next, segmented cells containing putative RNAscope and
512 immunofluorescent signals were determined to be positive or negative for associated
513 markers based on diameter and mean fluorescence intensity. Subsequent quantification

514 of counts was performed in R, while plotting and statistical analysis was performed in
515 GraphPad Prism software (Boston, MA).
516
517 **Inhibition of aPOA$^{Vglut2}$ neurons**
518 Hibernating hamsters were bilaterally injected with either AAV8-Samd3E-
519 hM4D(Gi)-P2A-nlsGFP or AAV8-Samd3E-EGFP-P2A-Synaptophysin-mRuby. On the
520 day of treatment, hamsters were aroused in the morning, I.P. injected with CLZ and
521 provided with CLZ water in the evening, I.P. injected again 16 hours later, and core body
522 temperature recorded. This regimen accounted for variability in water intake within the
523 first 24 hours of the experiment and maximized inhibition of our targeted population. A
524 CLZ water treatment window of 6 days (144 hours) was used. For PBS control treatment,
525 an identical regimen was followed.
526 **Temperature data analysis.** In GraphPad Prism (Boston, MA), absolute elapsed
527 time of euthermia from start of treatment was used to determine differences within groups.
528 The treatment window duration (144 hours) was applied as an upper bound for statistical
529 analysis. In R, temperature data from each virus group and treatment condition was
530 mapped to circadian time. In GraphPad Prism (Boston, MA), statistical analysis was
531 performed on temperatures in the light and dark cycles within virus groups.
532
533 **Excitation of aPOA$^{Vglut2}$ neurons**
534 Hamsters were bilaterally injected with either AAV8-Samd3E-hM3D(Gq)-P2A-
535 nlsGFP or AAV8-Samd3E-EGFP-P2A-Synaptophysin-mRuby and housed at 4°C to
536 acclimate. On the day of treatment, hamsters were aroused in the morning, I.P. injected

537 with CLZ in the evening, and core body temperature recorded. For PBS control treatment,
538 an identical regimen was followed.

539 **Temperature data analysis.** In R, temperature data was analyzed using the
540 method described in section 'Torpor bout analysis' to determine if the CLZ induced drop
541 in body temperature clustered with either deep or shallow torpor. In GraphPad Prism
542 (Boston, MA), statistical analysis was performed on minimum temperatures across each
543 condition (euthermia, torpor, CLZ, and PBS).

544 **Sample imaging.** Collected brains were processed as indicated in the section
545 'Immunofluorescence' using the following reagent for the detection of AAV8-Samd3E-
546 hM3D(Gq)-P2A-nlsGFP: Chicken anti-GFP, Aves Labs, GFP-1020. Sections were
547 imaged with a TissueFAXS SL whole-slide scanning system equipped with a Zeiss Axio
548 Imager Z2 fluorescence microscope and TissueFAXS image acquisition software (Koch
549 Institute Swanson Biotechnology Center/Microscopy Core).

550 **Image and correlation analysis.** aPOA GFP expression was quantified in a semi
551 quantitative manner where expression was scored 0 (none), 1 (minimal), 2 (partial), or 3
552 (complete) in each hemisphere. The analysis was performed blinded to change in body
553 temperature observed in each hamster. Hemispheric values were summed within
554 animals. In GraphPad Prism (Boston, MA), a Pearson correlation was performed between
555 GFP viral expression and the minimum body temperature.

556

557 **Behavioral analysis**

558 Hamsters housed at 4°C and injected with AAV8-Samd3E-hM3D(Gq)-P2A-
559 nlsGFP or AAV8-Samd3E-EGFP-P2A-Synaptophysin-mRuby were I.P. injected with PBS

560 (0.5 mL/kg) after a one-hour baseline video recording of homecage behavior and an
561 additional hour recording post injection. Following at least a week recovery in 4°C
562 chambers, animals were injected with CLZ (5 mg/kg) and videos were recorded for one
563 hour before and post drug administration in 4°C chambers. Homecage behaviors were
564 manually coded using BORIS software[84]. Behavior was coded 30 min after PBS or CLZ
565 injection over a 10 min window.

566 **References**


567 1. Tan, C. L. & Knight, Z. A. Regulation of Body Temperature by the Nervous System.
568 *Neuron* **98**, 31–48 (2018).
569 2. Morrison, S. F. & Nakamura, K. Central Mechanisms for Thermoregulation. *Annu.*
570 *Rev. Physiol.* **81**, 285–308 (2019).
571 3. Heller, H. C. & Hammel, H. T. CNS control of body temperature during hibernation.
572 *Comp. Biochem. Physiol. A Physiol.* **41**, 349–359 (1972).
573 4. Sunagawa, G. A. & Takahashi, M. Hypometabolism during Daily Torpor in Mice is
574 Dominated by Reduction in the Sensitivity of the Thermoregulatory System. *Sci.*
575 *Rep.* **6**, 1–14 (2016).
576 5. Geiser, F. Metabolic Rate and Body Temperature Reduction During Hibernation and
577 Daily Torpor. *Annu. Rev. Physiol.* **66**, 239–274 (2004).
578 6. Geiser, F. *Ecological Physiology of Daily Torpor and Hibernation*. (Springer, Cham,
579 Switzerland, 2021).
580 7. Drew, K. L. *et al.* Central nervous system regulation of mammalian hibernation:
581 implications for metabolic suppression and ischemia tolerance. *J Neurochem* **102**,
582 1713–1726 (2007).
583 8. Heller, H. C. Hibernation: neural aspects. *Annu. Rev. Physiol.* **41**, 305–321 (1979).
584 9. Morton, S. R. Torpor and Nest-Sharing in Free-Living Sminthopsis crassicaudata
585 (Marsupialia) and Mus musculus (Rodentia). *J. Mammal.* **59**, 569–575 (1978).
586 10. Swoap, S. J. & Gutilla, M. J. Cardiovascular changes during daily torpor in the
587 laboratory mouse. *Am. J. Physiol.-Regul. Integr. Comp. Physiol.* **297**, R769–R774
588 (2009).

589 11. Barnes, B. M. Freeze avoidance in a mammal: body temperatures below 0 degree C
590 in an Arctic hibernator. *Science* **244**, 1593–1595 (1989).
591 12. Heldmaier, G., Ortmann, S. & Elvert, R. Natural hypometabolism during hibernation
592 and daily torpor in mammals. *Respir. Physiol. Neurobiol.* **141**, 317–329 (2004).
593 13. Revel, F. G. *et al.* The circadian clock stops ticking during deep hibernation in the
594 European hamster. *Proc. Natl. Acad. Sci.* **104**, 13816–13820 (2007).
595 14. Mohr, S. M., Bagriantsev, S. N. & Gracheva, E. O. Cellular, Molecular, and
596 Physiological Adaptations of Hibernation: The Solution to Environmental
597 Challenges. *Annu. Rev. Cell Dev. Biol.* **36**, 315–338 (2020).
598 15. Chayama, Y., Ando, L., Tamura, Y., Miura, M. & Yamaguchi, Y. Decreases in body
599 temperature and body mass constitute pre-hibernation remodelling in the Syrian
600 golden hamster, a facultative mammalian hibernator. *R. Soc. Open Sci.* **3**, 160002
601 (2016).
602 16. Teague, R. S. & Ranson, S. W. The role of the anterior hypothalamus in
603 temperature regulation. *Am. J. Physiol.-Leg. Content* **117**, 562–570 (1936).
604 17. Hammel, H. T. & Pierce, J. B. Regulation of Internal Body Temperature. *Annu. Rev.*
605 *Physiol.* **30**, 641–710 (1968).
606 18. Zaretskaia, M. V., Zaretsky, D. V., Shekhar, A. & DiMicco, J. A. Chemical stimulation
607 of the dorsomedial hypothalamus evokes non-shivering thermogenesis in
608 anesthetized rats. *Brain Res.* **928**, 113–125 (2002).
609 19. Nakamura, K. & Morrison, S. F. A thermosensory pathway that controls body
610 temperature. *Nat Neurosci* **11**, 62–71 (2008).

611 20. Hensel, H. Neural processes in thermoregulation. *Physiol. Rev.* **53**, 948–1017
612 (1973).
613 21. Jessen, C. Thermal afferents in the control of body temperature. *Pharmacol. Ther.*
614 **28**, 107–134 (1985).
615 22. Hammel, H. T., Hardy, J. D. & Fusco, M. M. Thermoregulatory responses to
616 hypothalamic cooling in unanesthetized dogs. *Am J Physiol* **198**, 481–6 (1960).
617 23. Magoun, H. W., Harrison, F., Brobeck, J. R. & Ranson, S. W. Activation of heat loss
618 mechanisms by local heating of the brain. *J. Neurophysiol.* **1**, 101–114 (1938).
619 24. Tan, C. L. *et al.* Warm-Sensitive Neurons that Control Body Temperature. *Cell* **167**,
620 47-59.e15 (2016).
621 25. Song, K. *et al.* The TRPM2 channel is a hypothalamic heat sensor that limits fever
622 and can drive hypothermia. *Science* **353**, 1393–1398 (2016).
623 26. Yu, S. *et al.* Glutamatergic Preoptic Area Neurons That Express Leptin Receptors
624 Drive Temperature-Dependent Body Weight Homeostasis. *J Neurosci* **36**, 5034–46
625 (2016).
626 27. Zhou, Q. *et al.* Hypothalamic warm-sensitive neurons require TRPC4 channel for
627 detecting internal warmth and regulating body temperature in mice. *Neuron* **111**,
628 387-404 e8 (2023).
629 28. Vitale, P. M., Darrow, J. M., Duncan, M. J., Shustak, C. A. & Goldman, B. D. Effects
630 of photoperiod, pinealectomy and castration on body weight and daily torpor in
631 Djungarian hamsters (Phodopus sungorus). *J. Endocrinol.* **106**, 367–375 (1985).

632 29. Paul, M. J., Kauffman, A. S. & Zucker, I. Feeding schedule controls circadian timing
633 of daily torpor in SCN-ablated Siberian hamsters. *J. Biol. Rhythms* **19**, 226–237
634 (2004).
635 30. Magariños, A. M., McEwen, B. S., Saboureau, M. & Pevet, P. Rapid and reversible
636 changes in intrahippocampal connectivity during the course of hibernation in
637 European hamsters. *Proc. Natl. Acad. Sci. U. S. A.* **103**, 18775–18780 (2006).
638 31. Korhonen, T., Mustonen, A.-M., Nieminen, P. & Saarela, S. Effects of cold exposure,
639 exogenous melatonin and short-day treatment on the weight-regulation and body
640 temperature of the Siberian hamster (Phodopus sungorus). *Regul. Pept.* **149**, 60–66
641 (2008).
642 32. Stanton, T. L., Daley, J. C. & Salzman, S. K. Prolongation of hibernation bout
643 duration by continuous intracerebroventricular infusion of melatonin in hibernating
644 ground squirrels. *Brain Res.* **413**, 350–355 (1987).
645 33. Chmura, H. E. *et al.* Hypothalamic remodeling of thyroid hormone signaling during
646 hibernation in the arctic ground squirrel. *Commun. Biol.* **5**, 492 (2022).
647 34. Tamura, Y., Shintani, M., Nakamura, A., Monden, M. & Shiomi, H. Phase-specific
648 central regulatory systems of hibernation in Syrian hamsters. *Brain Res.* **1045**, 88–
649 96 (2005).
650 35. Olson, J. M. *et al.* Circannual rhythm in body temperature, torpor, and sensitivity to
651 $A_1$ adenosine receptor agonist in arctic ground squirrels. *J. Biol. Rhythms* **28**, 201–
652 207 (2013).

653 36. Jinka, T. R., Tøien, Ø. & Drew, K. L. Season primes the brain in an arctic hibernator
654 to facilitate entrance into torpor mediated by adenosine A(1) receptors. *J. Neurosci.*
655 *Off. J. Soc. Neurosci.* **31**, 10752–10758 (2011).
656 37. Frare, C., Jenkins, M. E., Soldin, S. J. & Drew, K. L. The Raphe Pallidus and the
657 Hypothalamic-Pituitary-Thyroid Axis Gate Seasonal Changes in Thermoregulation in
658 the Hibernating Arctic Ground Squirrel (Urocitellus parryii). *Front. Physiol.* **9**, 1747
659 (2018).
660 38. Stanton, T. L., Winokur, A. & Beckman, A. L. Seasonal variation in thyrotropin-
661 releasing hormone (TRH) content of different brain regions and the pineal in the
662 mammalian hibernator, Citellus lateralis. *Regul. Pept.* **3**, 135–144 (1982).
663 39. Mohr, S. M. *et al.* Hypothalamic hormone deficiency enables physiological anorexia
664 in ground squirrels during hibernation. *Nat. Commun.* **15**, 5803 (2024).
665 40. Harris, M. B. & Milsom, W. K. Parasympathetic influence on heart rate in euthermic
666 and hibernating ground squirrels. *J. Exp. Biol.* **198**, 931–937 (1995).
667 41. Markussen, F. A. F., Cazarez-Marquez, F., Melum, V. J., Hazlerigg, D. G. & Wood,
668 S. H. c-fos induction in the choroid plexus, tanycytes and pars tuberalis is an early
669 indicator of spontaneous arousal from torpor in a deep hibernator. *J Exp Biol* **227**,
670 (2024).
671 42. Enoki, R. *et al.* Cold-induced suspension and resetting of Ca2+ and transcriptional
672 rhythms in the suprachiasmatic nucleus neurons. *iScience* **26**, 108390 (2023).
673 43. Cheng, M. *et al.* Brainstem catecholaminergic neurons induce torpor during fasting
674 by orchestrating cardiovascular and thermoregulation changes. *Nat. Commun.* **16**,
675 5954 (2025).

676 44. Bratincsak, A. *et al.* Spatial and temporal activation of brain regions in hibernation: c-
677 fos expression during the hibernation bout in thirteen-lined ground squirrel. *J Comp*
678 *Neurol* **505**, 443–58 (2007).
679 45. Weidler, D. J., Earle, A. M., Myers, G. G. & Sieck, G. C. Effect of hypothalamic
680 lesions on temperature regulation in hibernating ground squirrels. *Brain Res.* **65**,
681 175–179 (1974).
682 46. Hastings, M. H., Maywood, E. S. & Brancaccio, M. Generation of circadian rhythms
683 in the suprachiasmatic nucleus. *Nat. Rev. Neurosci.* **19**, 453–469 (2018).
684 47. Welsh, D. K., Takahashi, J. S. & Kay, S. A. Suprachiasmatic Nucleus: Cell
685 Autonomy and Network Properties. *Annu. Rev. Physiol.* **72**, 551–577 (2010).
686 48. Weaver, D. R. The Suprachiasmatic Nucleus: A 25-Year Retrospective. *J. Biol.*
687 *Rhythms* **13**, 100–112 (1998).
688 49. Andermann, M. L. & Lowell, B. B. Toward a Wiring Diagram Understanding of
689 Appetite Control. *Neuron* **95**, 757–778 (2017).
690 50. Cone, R. D. *et al.* The arcuate nucleus as a conduit for diverse signals relevant to
691 energy homeostasis. *Int. J. Obes.* **25**, S63–S67 (2001).
692 51. Jais, A. & Brüning, J. C. Arcuate Nucleus-Dependent Regulation of Metabolism—
693 Pathways to Obesity and Diabetes Mellitus. *Endocr. Rev.* **43**, 314–328 (2022).
694 52. Van der Werf, Y. D., Witter, M. P. & Groenewegen, H. J. The intralaminar and
695 midline nuclei of the thalamus. Anatomical and functional evidence for participation
696 in processes of arousal and awareness. *Brain Res. Rev.* **39**, 107–140 (2002).
697 53. Jones, B. E. Arousal systems. *Front. Biosci. J. Virtual Libr.* **8**, s438-451 (2003).
698 54. Roth, B. L. DREADDs for Neuroscientists. *Neuron* **89**, 683–694 (2016).

699 55. Hrvatin, S. *et al.* Neurons that regulate mouse torpor. *Nature* **583**, 115–121 (2020).
700 56. Takahashi, T. M. *et al.* A discrete neuronal circuit induces a hibernation-like state in
701 rodents. *Nature* **583**, 109–114 (2020).
702 57. Zhang, Z. *et al.* Estrogen-sensitive medial preoptic area neurons coordinate torpor in
703 mice. *Nat. Commun.* **11**, 6378 (2020).
704 58. Machado, N. L. S. *et al.* Preoptic EP3R neurons constitute a two-way switch for
705 fever and torpor. *Nature* 1–10 (2025) doi:10.1038/s41586-025-09056-1.
706 59. Ambler, M., Hitrec, T., Wilson, A., Cerri, M. & Pickering, A. Neurons in the
707 Dorsomedial Hypothalamus Promote, Prolong, and Deepen Torpor in the Mouse. *J.*
708 *Neurosci. Off. J. Soc. Neurosci.* **42**, 4267–4277 (2022).
709 60. Kaplan, H. S. *et al.* Sensory input, sex and function shape hypothalamic cell type
710 development. *Nature* https://doi.org/10.1038/s41586-025-08603-0 (2025)
711 doi:10.1038/s41586-025-08603-0.
712 61. Zhang, M. *et al.* Molecularly defined and spatially resolved cell atlas of the whole
713 mouse brain. *Nature* **624**, 343–354 (2023).
714 62. Dimidschstein, J. *et al.* A viral strategy for targeting and manipulating interneurons
715 across vertebrate species. *Nat. Neurosci.* **19**, 1743–1749 (2016).
716 63. Cronin, T. *et al.* Efficient transduction and optogenetic stimulation of retinal bipolar
717 cells by a synthetic adeno-associated virus capsid and promoter. *EMBO Mol. Med.*
718 **6**, 1175–1190 (2014).
719 64. Ben-Simon, Y. *et al.* A suite of enhancer AAVs and transgenic mouse lines for
720 genetic access to cortical cell types. *Cell* **188**, 3045-3064 e23 (2025).

721 65. Graybuck, L. T. *et al.* Enhancer viruses for combinatorial cell-subclass-specific
722 labeling. *Neuron* **109**, 1449-1464.e13 (2021).
723 66. Hrvatin, S. *et al.* A scalable platform for the development of cell-type-specific viral
724 drivers. *eLife* **8**, e48089 (2019).
725 67. Nagy, M. A. *et al.* Cis-regulatory elements driving motor neuron-selective viral
726 payload expression within the mammalian spinal cord. *Proc. Natl. Acad. Sci.* **121**,
727 e2418024121 (2024).
728 68. Hunker, A. C. *et al.* Enhancer AAV toolbox for accessing and perturbing striatal cell
729 types and circuits. *Neuron* **113**, 1507-1524 e17 (2025).
730 69. Junkins, M. S., Bagriantsev, S. N. & Gracheva, E. O. Towards understanding the
731 neural origins of hibernation. *J. Exp. Biol.* **225**, jeb229542 (2022).
732 70. Lovegrove, B. G. A phenology of the evolution of endothermy in birds and mammals.
733 *Biol Rev Camb Philos Soc* **92**, 1213–1240 (2017).
734 71. Geiser, F., Stawski, C., Wacker, C. B. & Nowack, J. Phoenix from the Ashes: Fire,
735 Torpor, and the Evolution of Mammalian Endothermy. *Front Physiol* **8**, 842 (2017).
736 72. Kita, Y. *et al.* Cellular-resolution gene expression profiling in the neonatal marmoset
737 brain reveals dynamic species- and region-specific differences. *Proc. Natl. Acad.*
738 *Sci.* **118**, e2020125118 (2021).
739 73. Shimogori, T. *et al.* Digital gene atlas of neonate common marmoset brain.
740 *Neurosci. Res.* **128**, 1–13 (2018).
741 74. Gene Structural Search | Marmoset Gene Atlas. https://gene-
742 atlas.brainminds.jp/gene-structural/.

743 75. Trefna, M. *et al.* The influence of sex and diet on the characteristics of hibernation in
744 Syrian hamsters. *J. Comp. Physiol. [B]* **187**, 725–734 (2017).
745 76. Negrini, M., Wang, G., Heuer, A., Björklund, T. & Davidsson, M. AAV Production
746 Everywhere: A Simple, Fast, and Reliable Protocol for In-house AAV Vector
747 Production Based on Chloroform Extraction. *Curr. Protoc. Neurosci.* **93**, e103
748 (2020).
749 77. Wood, R. I. & Morin, L. P. *A Stereotaxic Atlas of the Golden Hamster Brain*.
750 (Elsevier Science, 2001).
751 78. Lopez, R., Regier, J., Cole, M. B., Jordan, M. I. & Yosef, N. Deep generative
752 modeling for single-cell transcriptomics. *Nat. Methods* **15**, 1053–1058 (2018).
753 79. Wolf, F. A., Angerer, P. & Theis, F. J. SCANPY: large-scale single-cell gene
754 expression data analysis. *Genome Biol.* **19**, 15 (2018).
755 80. Xu, C. *et al.* Probabilistic harmonization and annotation of single-cell transcriptomics
756 data with deep generative models. *Mol. Syst. Biol.* **17**, e9620 (2021).
757 81. Bravo González-Blas, C. *et al.* cisTopic: cis-regulatory topic modeling on single-cell
758 ATAC-seq data. *Nat. Methods* **16**, 397–400 (2019).
759 82. Bankhead, P. *et al.* QuPath: Open source software for digital pathology image
760 analysis. *Sci. Rep.* **7**, 16878 (2017).
761 83. Goldsborough, T. *et al.* A novel channel invariant architecture for the segmentation
762 of cells and nuclei in multiplexed images using InstanSeg. 2024.09.04.611150
763 Preprint at https://doi.org/10.1101/2024.09.04.611150 (2024).

764 84. Friard, O. & Gamba, M. BORIS: a free, versatile open-source event-logging software
765 for video/audio coding and live observations. *Methods Ecol. Evol.* **7**, 1325–1330
766 (2016).
767 85. Lein, E. S. *et al.* Genome-wide atlas of gene expression in the adult mouse brain.
768 *Nature* **445**, 168–176 (2007).
769

770 **Acknowledgments:** We thank M. Alkire, M.M. Chen, J.A. Cheng, and N.T. Nigrin for their
771 assistance with mouse experiments. We also thank additional Hrvatin lab members for
772 their thoughtful input on this project and manuscript. The snRNA-seq and snATAC-seq
773 were performed with the Whitehead Institute Genome Technology Core. Imaging was
774 performed either at the Ragon Institute Microscopy Core, Koch Institute Swanson
775 Biotechnology Center/Microscopy Core, or the Whitehead Institute W.M. Keck Facility for
776 Biological Imaging. This work was supported by the Mathers Foundation Grant, Searle
777 Scholars Program, Pew Charitable Trust, Longevity Impetus Grant from Norn Group,
778 Hevolution Foundation and Rosenkranz Foundation, MIT Research Support Committee
779 Grant, and Howard Hughes Medical Institute Hrabowski Scholar Program.
780 **Author Contributions:** A.J.M. and S.H. conceptualized the study and designed
781 experiments. A.J.M, C.M.R, A.J.L.P, W.L., A.S.L. performed and analyzed experiments.
782 E.C.G. and S.H. advised on the study and obtained funding for the research. A.J.M.,
783 E.C.G., and S.H. wrote the manuscript.
784 **Competing Interests:** Authors declare that they have no competing interests.
785 **Data and materials availability:** Data will be made available on GEO. All other data
786 needed to evaluate the conclusions are available in the main text, the extended data,
787 supplementary materials, and available upon request.

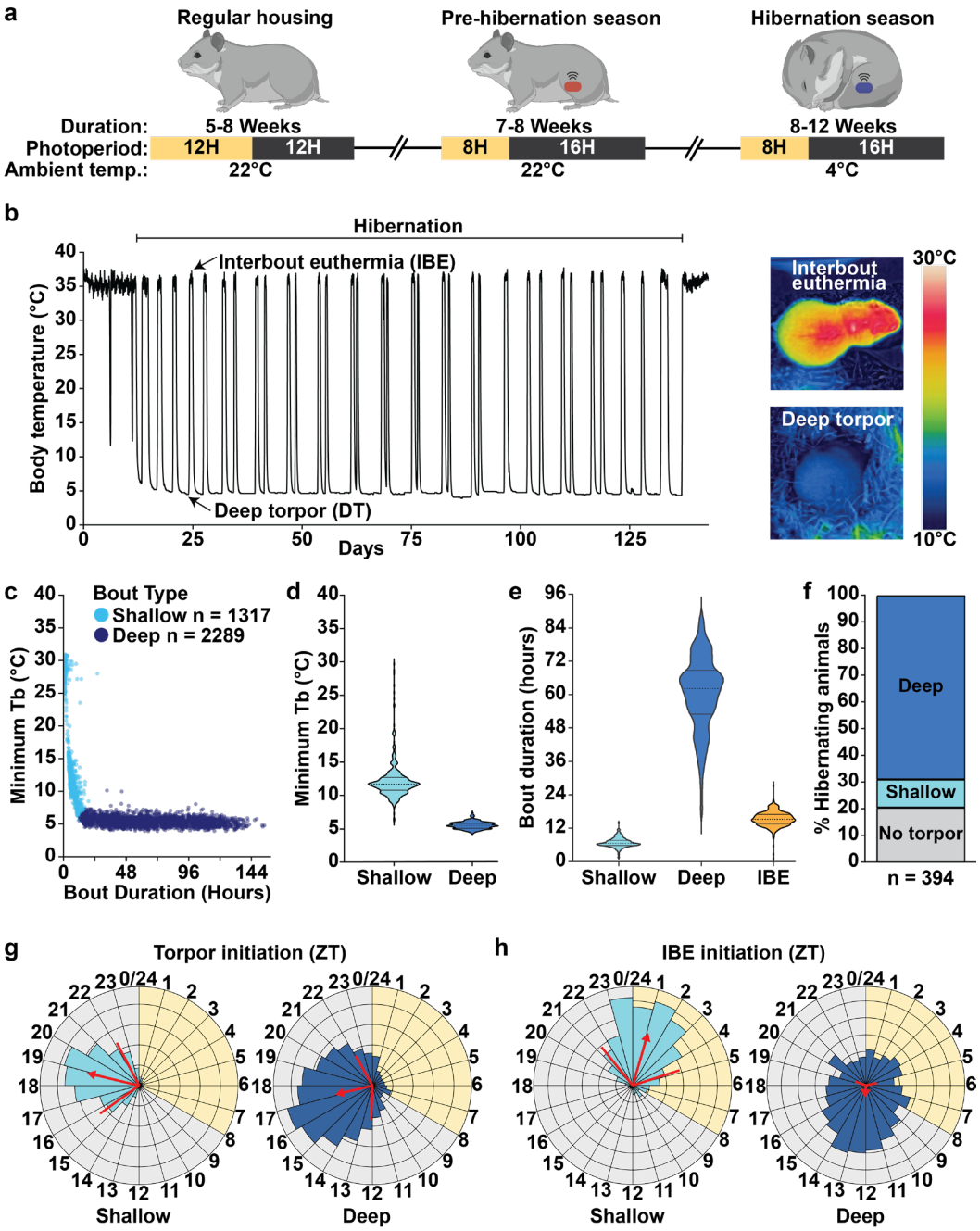


**Fig. 1: A laboratory model of Syrian hamster hibernation.**

**a**, A laboratory paradigm for hibernation induction in the Syrian hamster, transitioning animals to an altered light cycle and ambient temperature to simulate seasonal changes.

792 **b**, Representative body temperature trace of a hibernating hamster, consisting of
793 repeated bouts of deep torpor (DT) and interbout euthermia (IBE) (left). Thermal images
794 of a hibernating hamster during euthermic and deep torpor intervals (right).
795 **c**, Classification of torpor bouts as shallow (n = 1317) or deep (n = 2289) based on
796 minimum temperature and bout duration.
797 **d**,**e**, Violin plots of minimum body temperature (**d**), and duration (**e**) of shallow and deep
798 torpor bouts as well as IBE periods (n = 2471).
799 **f**, Percentage of animals undergoing DT, only shallow torpor, or no torpor bouts within 6
800 weeks of initiating the hibernation period (n = 394 animals).
801 **g**, Circadian representation (Raleigh plot) of the time of entry into shallow (light blue, n =
802 1312) or deep (dark blue, n = 2283) torpor bouts. Light and dark cycle phases are
803 represented by yellow and grey, respectively. Red arrow direction and length indicate
804 mean time of initiation and concentration around the mean, respectively. Red lines
805 flanking the arrow indicate s.d.
806 **h**, Circadian representation as in (**g**) of entry into IBE following deep (left, n = 1496) or
807 shallow (right, n = 1011) torpor bouts.

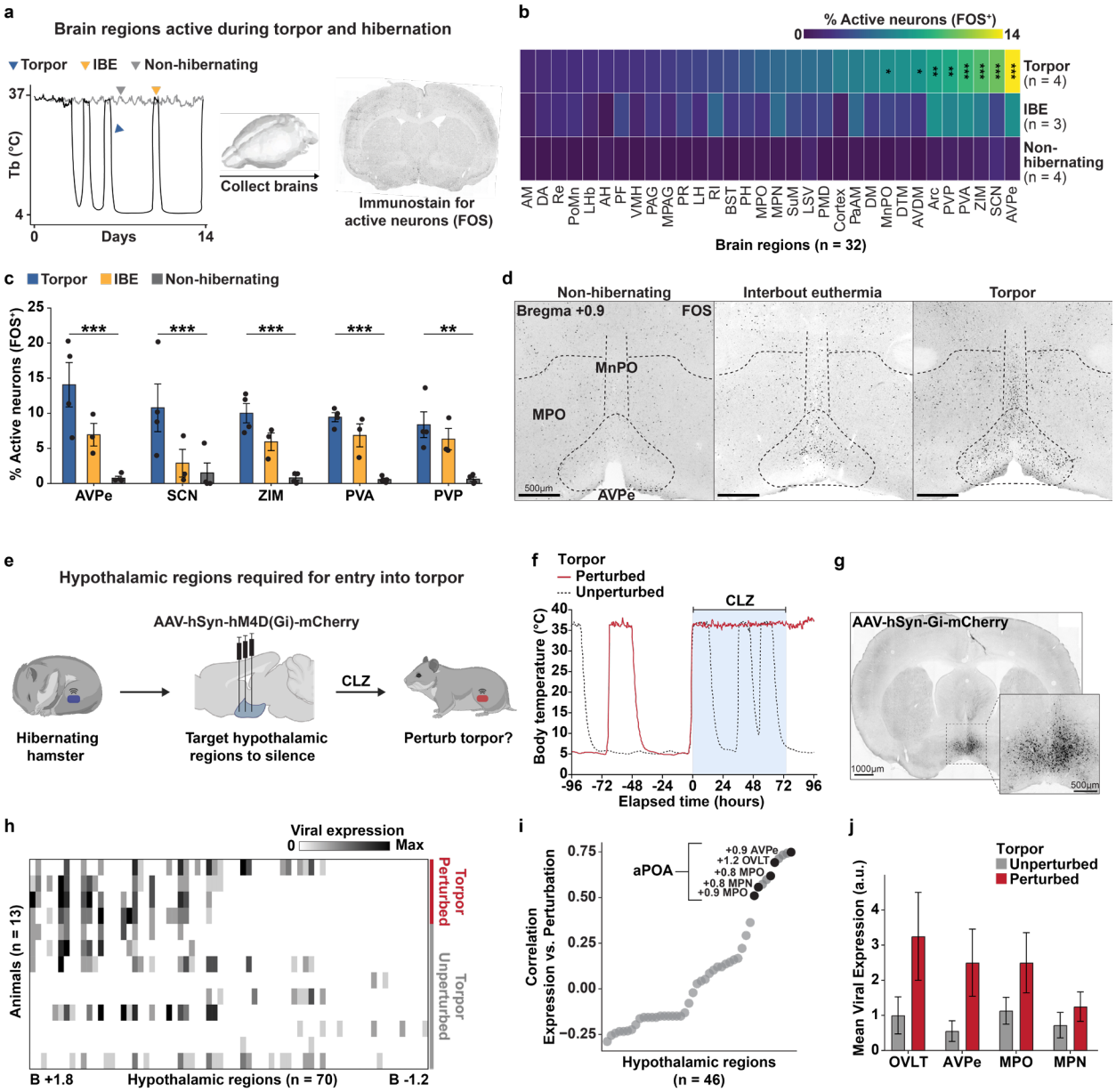


**Fig. 2: Identification and functional assessment of deep torpor-active brain regions.** **a**, Strategy for identifying brain regions with hibernation state-dependent activity. Arrows indicate relative sample collection points for torpor, IBE, and non-hibernating animals. **b**,**c**, Hypothalamic and thalamic regions demonstrating an increase in FOS-positive cells in torpor (n = 4 animals) as compared to both IBE (n = 3 animals) and non-hibernating (n = 4 animals) controls (*P-adjusted < 0.05, **P-adjusted < 0.01, ***P-adjusted < 0.001).

815 **d**, FOS immunostaining in the hamster POA across hibernation states. AVPe, MPO, and
816 MnPO denoted by dashed lines.
817 **e**, Strategy for identifying hypothalamic subregions regulating deep torpor entry.
818 **f**, $T_b$ traces showing CLZ-mediated disruption of DT in one Gi-DREADD-mCherry-
819 transduced hamster (solid red) but not the other (dashed black).
820 **g**, Coronal section and inset showing Gi-mCherry expression in the hypothalamus.
821 **h**, Quantification of regional viral Gi-mCherry expression across injected animals.
822 Hypothalamic regions (n = 70) plotted relative to bregma anterior-posterior coordinates.
823 **i**, Correlation of regional viral expression across animals with the degree of torpor
824 perturbation identifies the anterior POA (aPOA) as a key DT-regulating region.
825 **j**, Higher viral Gi-mCherry expression in aPOA regions from animals exhibiting CLZ-
826 dependent torpor disruption (n = 4) compared to unaffected animals (n = 13). Mean ±
827 s.e.m.

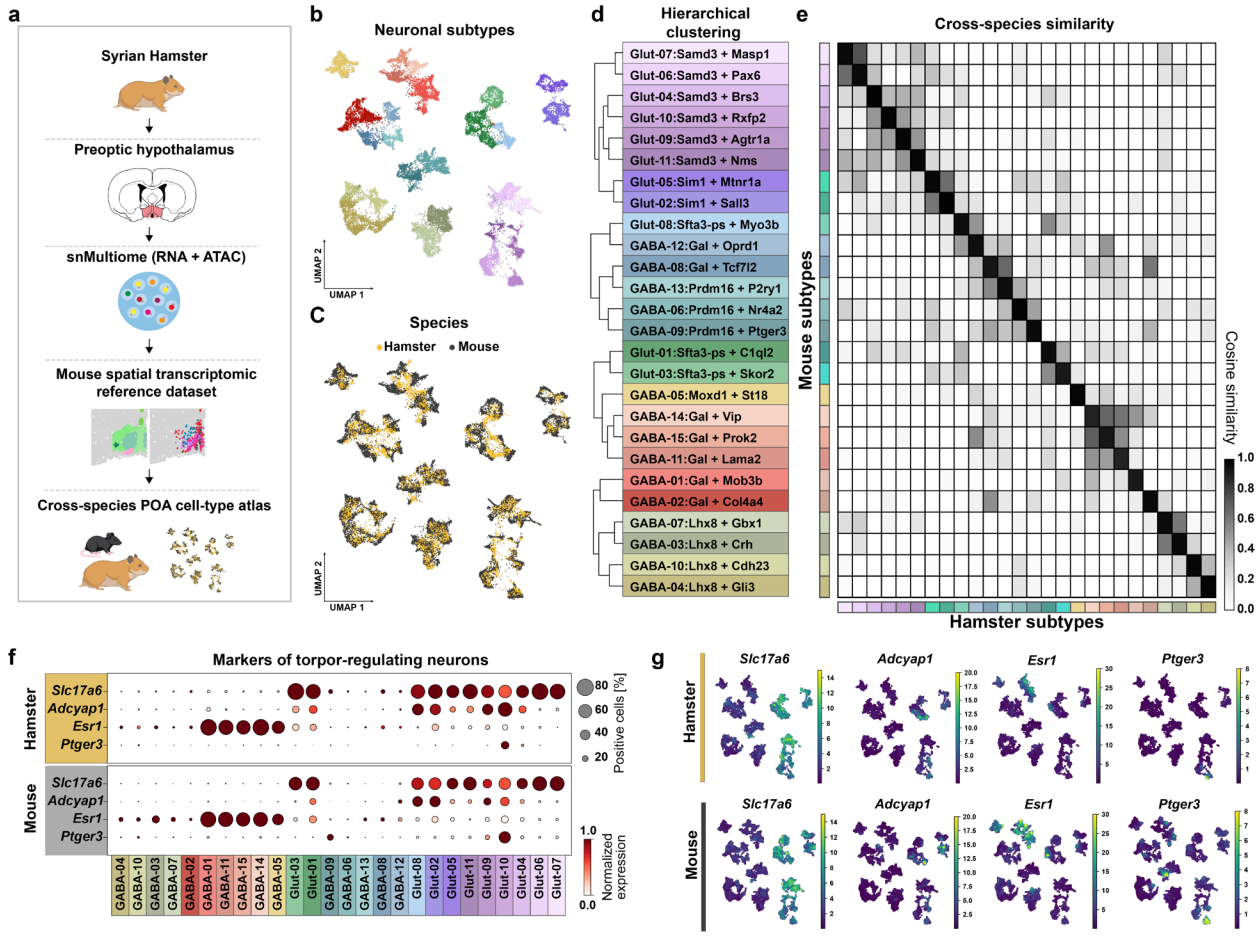
a
Syrian Hamster
Preoptic hypothalamus
snMultiome (RNA + ATAC)
Mouse spatial transcriptomic reference dataset
Cross-species POA cell-type atlas
b
Neuronal subtypes
UMAP 2
UMAP 1
c
Species
Hamster
Mouse
d
Hierarchical clustering
Glut-07:Samd3 + Masp1
Glut-06:Samd3 + Pax6
Glut-04:Samd3 + Brs3
Glut-10:Samd3 + Rxfp2
Glut-09:Samd3 + Agtr1a
Glut-11:Samd3 + Nms
Glut-05:Sim1 + Mtnr1a
Glut-02:Sim1 + Sall3
Glut-08:Sfta3-ps + Myo3b
GABA-12:Gal + Oprd1
GABA-08:Gal + Tcf7l2
GABA-13:Prdm16 + P2ry1
GABA-06:Prdm16 + Nr4a2
GABA-09:Prdm16 + Ptger3
Glut-01:Sfta3-ps + C1ql2
Glut-03:Sfta3-ps + Skor2
GABA-05:Moxd1 + St18
GABA-14:Gal + Vip
GABA-15:Gal + Prok2
GABA-11:Gal + Lama2
GABA-01:Gal + Mob3b
GABA-02:Gal + Col4a4
GABA-07:Lhx8 + Gbx1
GABA-03:Lhx8 + Crh
GABA-10:Lhx8 + Cdh23
GABA-04:Lhx8 + Gli3
e
Cross-species similarity
Mouse subtypes
Hamster subtypes
Cosine similarity
1.0
0.8
0.6
0.4
0.2
0.0
f
Markers of torpor-regulating neurons
Hamster
Mouse
Slc17a6
Adcyap1
Esr1
Ptger3
Positive cells [%]
80
60
40
20
Normalized expression
1.0
0.0
GABA-04
GABA-10
GABA-03
GABA-07
GABA-02
GABA-01
GABA-11
GABA-15
GABA-14
GABA-05
Glut-03
Glut-01
GABA-09
GABA-06
GABA-13
GABA-08
GABA-12
Glut-08
Glut-02
Glut-05
Glut-11
Glut-09
Glut-10
Glut-04
Glut-06
Glut-07
g
Hamster
Mouse
Slc17a6
Adcyap1
Esr1
Ptger3
h
Hamster anterior POA
Vglut2
Adcyap1
B +1.3
+1.1
+0.9
100µm
10µm
i
Hamster torpor-active neurons
Vglut2
FOS
Adcyap1
FOS
500µm
50µm
j
% Colocalization FOS+Marker+/FOS+
100
90
80
70
60
50
40
30
20
10
0
Vglut2
Adcyap1
k
Regional separation of subtypes
UMAP 2
UMAP 1
aPOA^Vglut2
cPOA^Vglut2
aPOA^Vgat
cPOA^Vgat
l
Hamster Samd3 expression
Mouse Samd3 expression
m
Samd3 expression in torpor-active neurons
Samd3
FOS
500µm
50µm
n
% Colocalization FOS+Marker+/FOS+
100
90
80
70
60
50
40
30
20
10
0
Samd3

829 **Fig. 3: Cell taxonomy and activity mapping implicate glutamatergic aPOA neuronal**
830 **cell types in DT regulation.**

831 **a**, Workflow to generate a cross-species POA cellular taxonomy.

832 **b**,**c**, Uniform manifold approximation and projection (UMAP) plot showing 18,406 nuclei
833 from mice (n = 11) and 8,355 nuclei from Syrian Hamsters (n = 7), indicating 15
834 GABAergic and 11 glutamatergic neuronal subtypes (**b**) or species of origin (**c**).

835 **d**, Hierarchical clustering of the neuronal subtypes.

836 **e**, Cosine similarity analysis showing pairwise transcriptional relatedness between
837 hamster and mouse neuronal subtypes based on mean gene expression.

838 **f**, Dot plot showing FIT-associated marker gene expression across mouse and hamster
839 neuronal subtypes.

840 **g**, UMAP feature plots depicting marker gene expression in the indicated species.

841 **h**, ISH for select FIT-associated marker genes in hamster aPOA.

842 **i**,**j**, Combined FOS immunostaining and ISH analysis for *Slc17a6* (*Vglut2*) and *Adcyap1*
843 from aPOA of hamsters (n = 3) in DT, with accompanying quantification. Mean ± s.e.m.

844 **k**, UMAP plot annotating hamster and mouse POA neurons by regional location based
845 on mouse MERFISH data.

846 **l**, UMAP feature plots depicting *Samd3* expression in the indicated species.

847 **m**,**n**, Combined FOS immunostaining and *Samd3* ISH analysis of aPOA from hamsters
848 (n = 3) in DT, with accompanying quantification. Mean ± s.e.m.

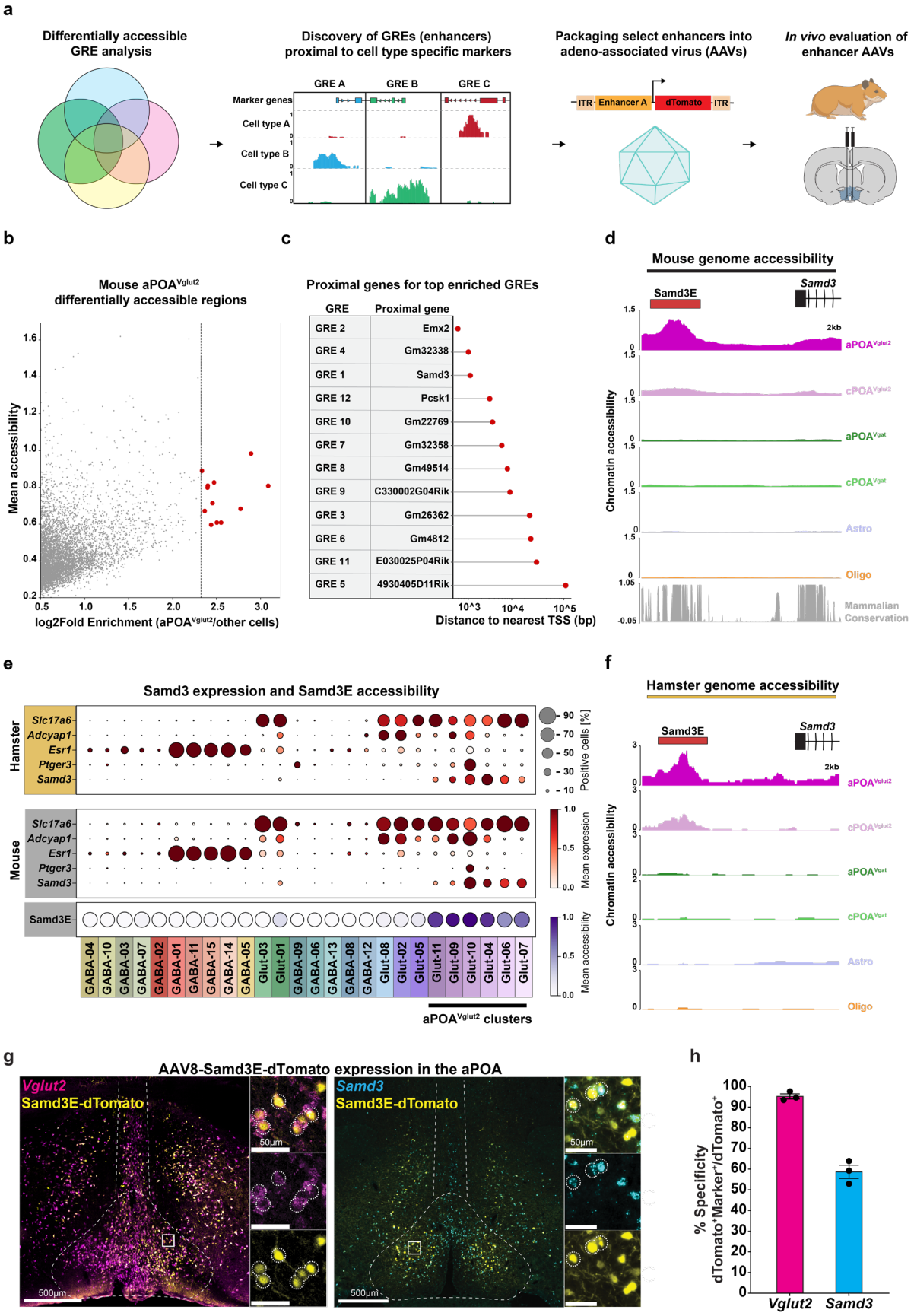
a
Differentially accessible GRE analysis
Discovery of GREs (enhancers) proximal to cell type specific markers
Packaging select enhancers into adeno-associated virus (AAVs)
In vivo evaluation of enhancer AAVs
GRE A
GRE B
GRE C
Marker genes
Cell type A
Cell type B
Cell type C
ITR
Enhancer A
dTomato
ITR
b
Mouse aPOAVglut2 differentially accessible regions
Mean accessibility
log2Fold Enrichment (aPOAVglut2/other cells)
c
Proximal genes for top enriched GREs
GRE
Proximal gene
GRE 2 Emx2
GRE 4 Gm32338
GRE 1 Samd3
GRE 12 Pcsk1
GRE 10 Gm22769
GRE 7 Gm32358
GRE 8 Gm49514
GRE 9 C330002G04Rik
GRE 3 Gm26362
GRE 6 Gm4812
GRE 11 E030025P04Rik
GRE 5 4930405D11Rik
Distance to nearest TSS (bp)
d
Mouse genome accessibility
Samd3E
Samd3
2kb
aPOAVglut2
cPOAVglut2
aPOAVgat
cPOAVgat
Astro
Oligo
Mammalian Conservation
Chromatin accessibility
e
Samd3 expression and Samd3E accessibility
Hamster
Mouse
Slc17a6
Adcyap1
Esr1
Ptger3
Samd3
Samd3E
Positive cells [%]
Mean expression
Mean accessibility
GABA-04 GABA-10 GABA-03 GABA-07 GABA-02 GABA-01 GABA-11 GABA-15 GABA-14 GABA-05 Glut-03 Glut-01 GABA-09 GABA-06 GABA-13 GABA-08 GABA-12 Glut-08 Glut-02 Glut-05 Glut-11 Glut-09 Glut-10 Glut-04 Glut-06 Glut-07
aPOAVglut2 clusters
f
Hamster genome accessibility
Samd3E
Samd3
2kb
aPOAVglut2
cPOAVglut2
aPOAVgat
cPOAVgat
Astro
Oligo
Chromatin accessibility
g
AAV8-Samd3E-dTomato expression in the aPOA
Vglut2
Samd3E-dTomato
Samd3
Samd3E-dTomato
50µm
500µm
h
% Specificity
dTomato+Marker+/dTomato+
Vglut2
Samd3

850 **Fig. 4: A novel Enhancer-AAV specifically targeting hamster aPOA$^{Vglut2}$ neurons.**

851 **a**, Workflow for generation of aPOA$^{Vglut2}$ neuron-selective enhancer-AAVs.

852 **b**, Scatter plot of genomic elements (n = 15,208) based on differential accessibility in
853 aPOA$^{Vglut2}$ neurons and mean aPOA$^{Vglut2}$ accessibility signal. Top 10 most differentially
854 accessible elements (FDR-corrected $q < 10^{-300}$) highlighted in red.

855 **c**, Distance to proximal gene transcription start site for the top 10 putative GREs from (**b**).

856 **d**, ATAC-seq genome browser tracks (normalized counts per location) for the mouse
857 *Samd3*-proximal putative GRE (*Samd3E,* red box) in the indicated cell populations in
858 mouse, with accompanying sequence conservation below.

859 **e**, Dotplot depicting *Samd3* gene expression across mouse and hamster POA neuronal
860 subtypes, along with *Samd3E* accessibility in the mouse.

861 **f**, ATAC-seq genome browser tracks (normalized counts per location) for the hamster
862 *Samd3*-proximal putative GRE (*Samd3E*, red box) in the indicated cell populations in
863 hamster.

864 **g**,**h**, Combined immunostaining for viral dTomato and ISH analysis for *Slc17a6* (*Vglut2*)
865 and *Samd3* from aPOA of hamsters injected with AAV8-Samd3E-dTomato, with
866 accompanying quantification. Mean ± s.e.m. (n = 3 animals).

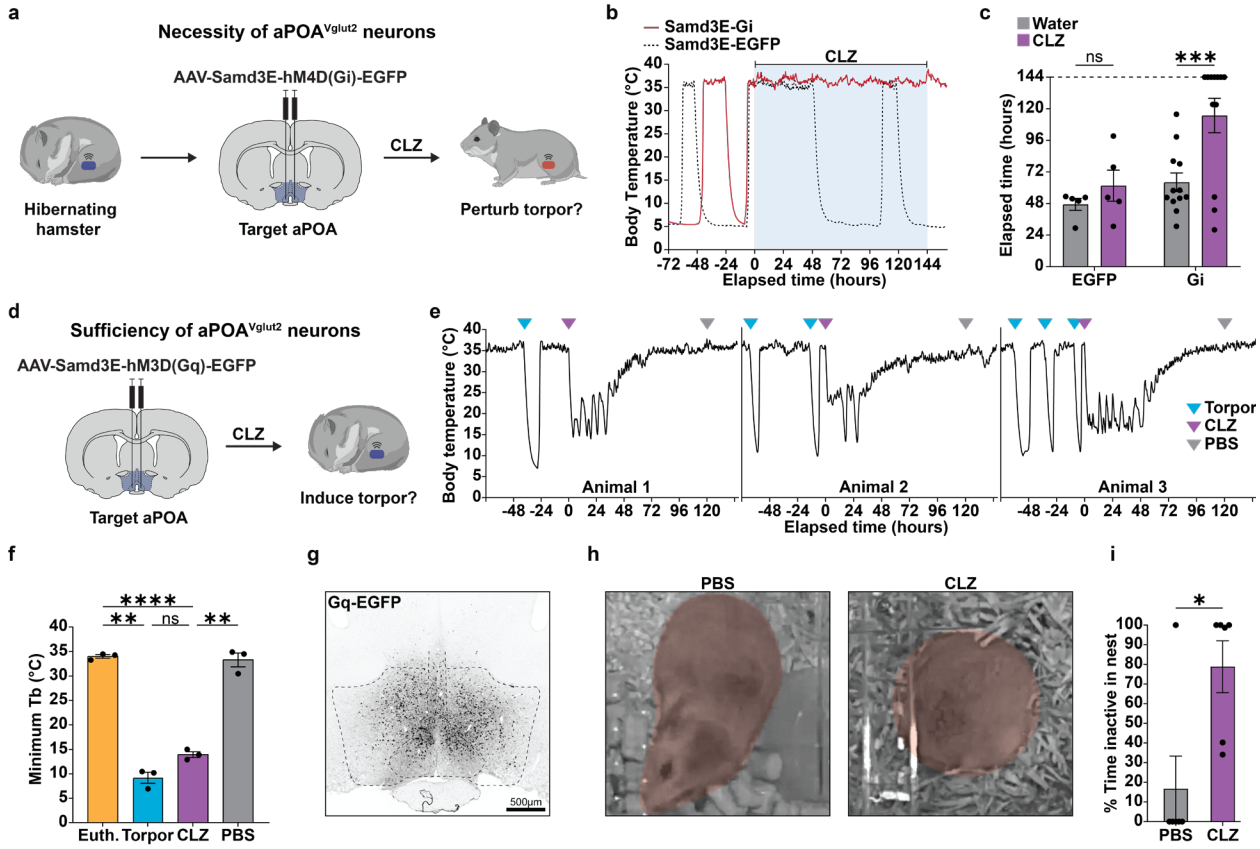


**Fig. 5: aPOA$^{Vglut2}$ neuronal activity is necessary and sufficient for hamster deep torpor entry.**

**a**, Strategy for testing the necessity of aPOA$^{Vglut2}$ neuronal activity for DT reentry.

**b**, $T_b$ traces demonstrating perturbation of torpor resumption upon CLZ administration in Samd3E-Gi-DREADD- but not control Samd3E-EGFP-transduced hamsters.

**c**, Samd3E-Gi-DREADD-transduced hamsters (n = 12), but not control Samd3E-EGFP-transduced animals (n = 5), show significant perturbations in torpor initiation when administered with CLZ but not water (Šídák's multiple comparisons test).

**d**, Strategy for testing the sufficiency of aPOA$^{Vglut2}$ neuronal activity for DT entry.

**e**, $T_b$ traces from Samd3E-Gq-DREADD-injected animals illustrating natural torpor bouts as well as artificial bouts elicited by CLZ administration.

879 **f**, Quantification of minimum $T_b$ reached in Samd3E-Gq-DREADD-transduced animals
880 during euthermic periods, natural deep torpor, and following administration of CLZ or
881 control PBS (n = 3, Tukey's multiple comparisons test).
882 **g**, Coronal section showing Samd3E-Gq-DREADD-EGFP expression in the hamster
883 aPOA.
884 **h**, Images of a Samd3E-Gq-DREADD-transduced hamster following PBS or CLZ
885 treatment.
886 **i**, Percentage of time Samd3E-Gq-DREADD-transduced animals (n = 6) spent inactive in
887 the nest over a 10 min observation window CLZ or control PBS administration (paired t-
888 test).
889 ****P-adjusted < 0.0001, ***P-adjusted < 0.001, **P-adjusted < 0.01, *P-adjusted < 0.05,
890 ns = not significant).

## Extended Data

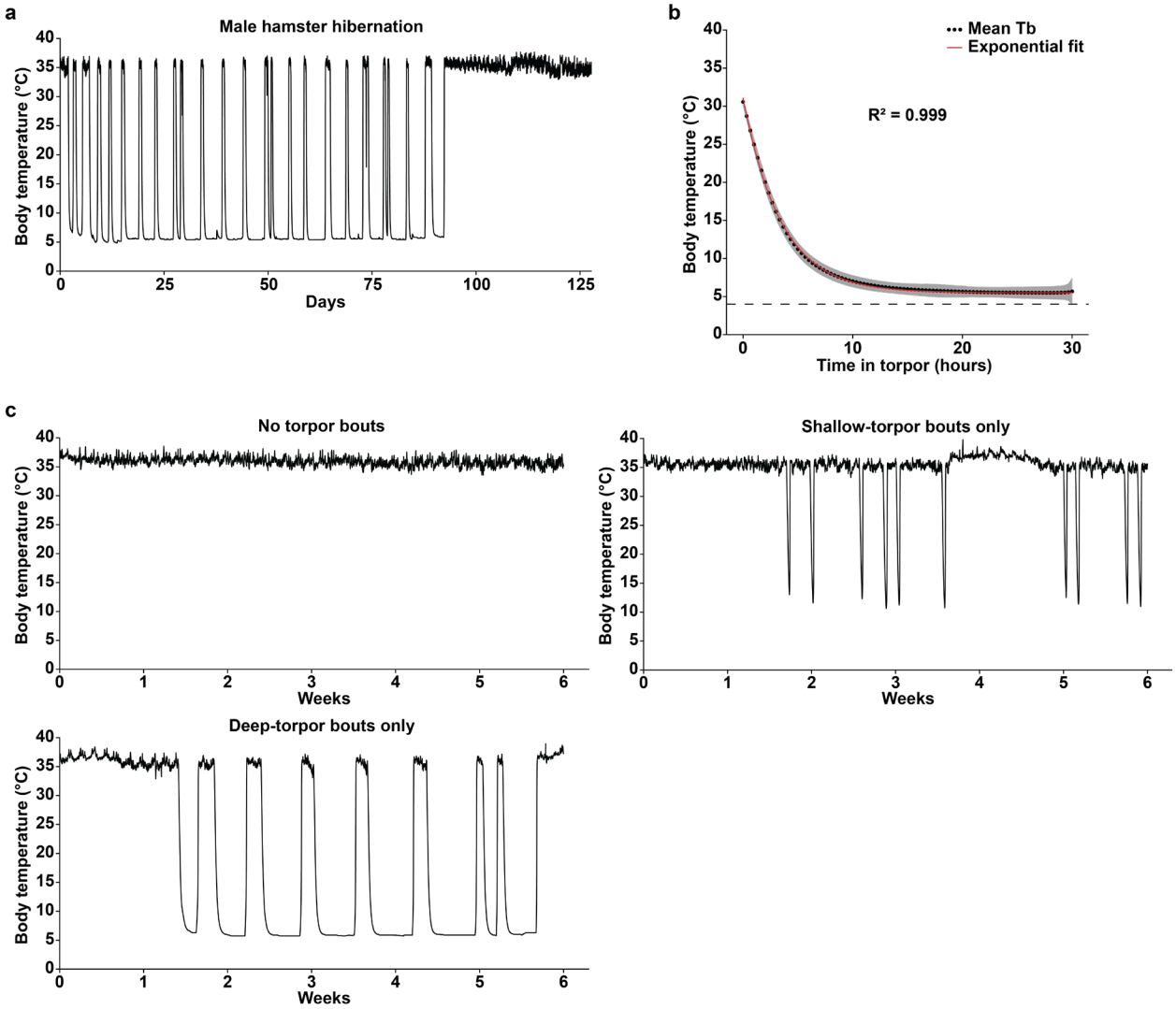


**Extended Data Fig. 1 Core body temperature dynamics during hibernation.**

**a**, Representative core body temperature trace from a male hamster across its hibernation season.

**b**, Initial $T_b$ decreases during torpor onset follow an exponential decay (animals = 188, torpor bouts = 1262).

**c**, Body temperature traces from three animals within a 6-week observation period, demonstrating the range of $T_b$ changes.

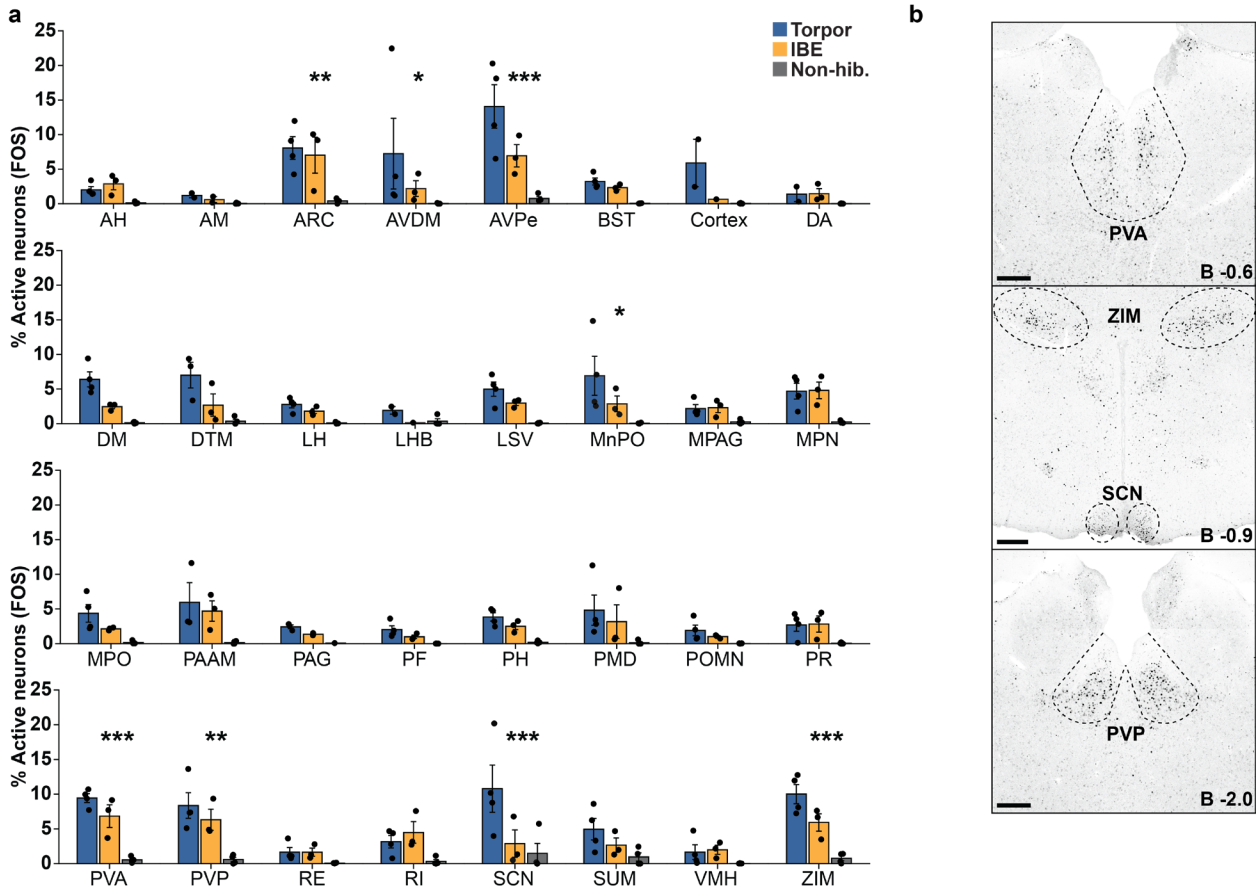
a
Torpor
IBE
Non-hib.
% Active neurons (FOS)
AH
AM
ARC
AVDM
AVPe
BST
Cortex
DA
DM
DTM
LH
LHB
LSV
MnPO
MPAG
MPN
MPO
PAAM
PAG
PF
PH
PMD
POMN
PR
PVA
PVP
RE
RI
SCN
SUM
VMH
ZIM
b
PVA
B -0.6
ZIM
SCN
B -0.9
PVP
B -2.0

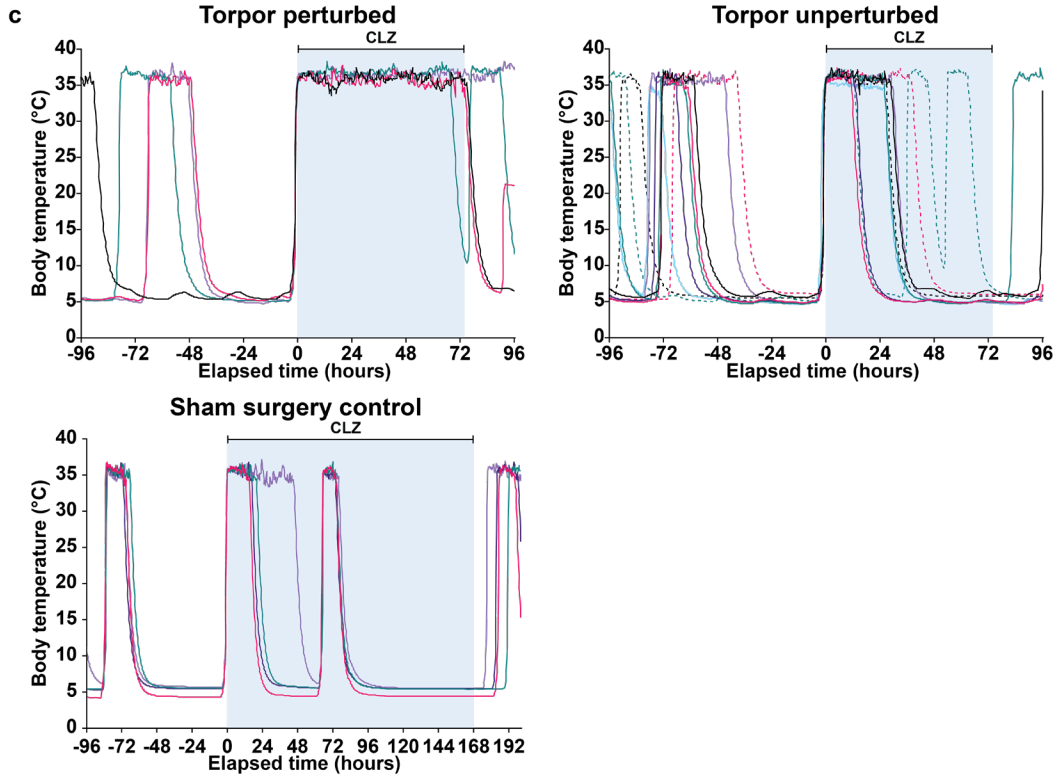
c
Torpor perturbed
Torpor unperturbed
Sham surgery control
CLZ
Body temperature (°C)
Elapsed time (hours)

**Extended Data Fig. 2 Hibernation-associated neuronal activity and disruption of torpor entry during targeted silencing.**

**a**, Bar plots showing the percentage of FOS-expressing neurons across all surveyed regions (n = 32) and hibernation stages (non-hibernating = 3 animals, IBE = 3 animals, torpor = 4 animals, p-adjusted < 0.05, **p-adjusted < 0.01, ***p-adjusted < 0.001). Data presented as mean ± s.e.m.

**b**, Representative FOS immunostaining images of an animal in torpor. The top four deep torpor-active regions after the AVPe are shown: Paraventricular thalamic nucleus anterior (PVA), zona incerta (ZIM), suprachiasmatic nucleus (SCN), and paraventricular thalamic nucleus posterior (PVP).

**c**, Hibernating hamsters (n = 13) were injected with AAV-hSyn-hM4D(Gi)-mCherry, targeting different areas of the anterior hypothalamus. After recovery of DT bouts, clozapine (CLZ, 5 mg/kg) was administered via drinking water. Hamster core body temperature traces are shown, demonstrating CLZ-dependent perturbation of torpor activity in a subset of animals (n = 4) while torpor entry remains unaffected in other animals (n = 9).

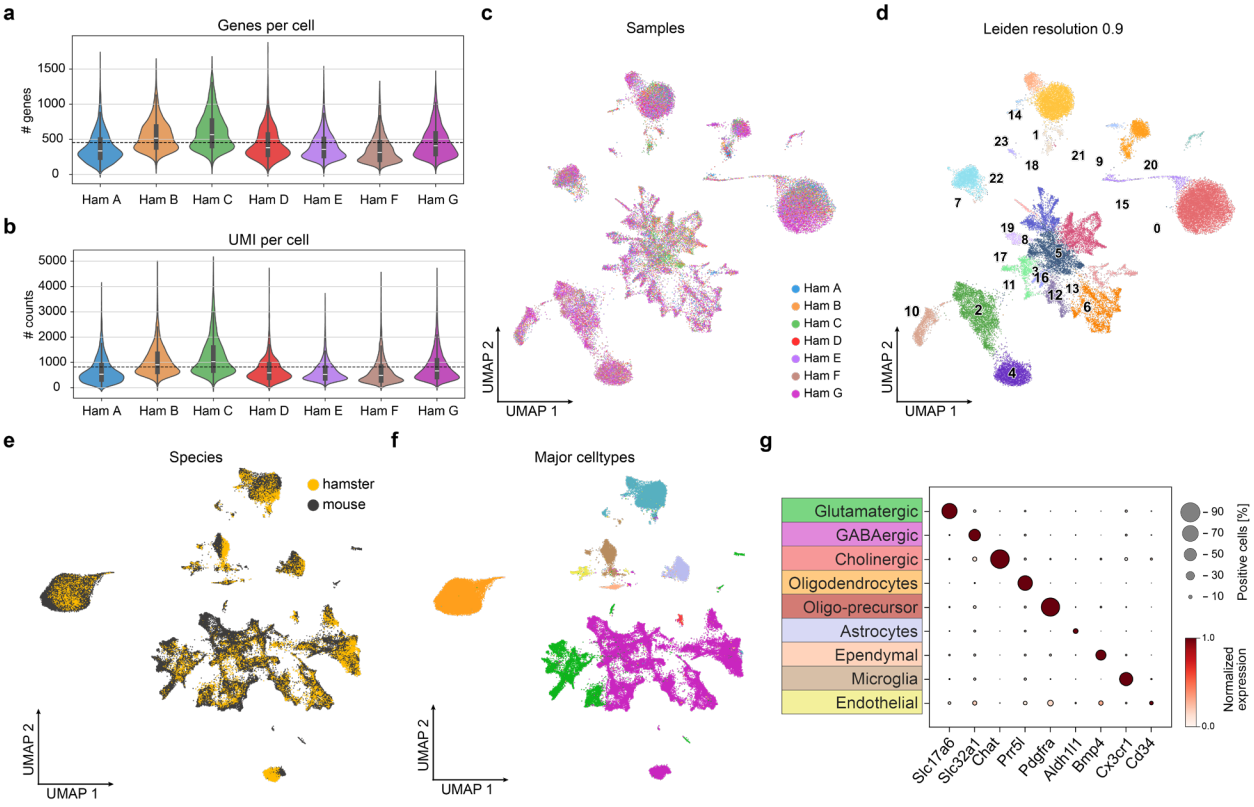


**Extended Data Fig. 3 snRNA-seq analysis of hamster and mouse POA and separation of major neuronal and non-neuronal cell types.**

Our snRNA-seq and snATAC-seq data from hamster POA samples were first aligned with the mouse POA multiome dataset from Kaplan et. al[60], separating major neuronal and non-neuronal cell types from both datasets.

**a**,**b**, Violin plots showing the number of detected genes (**a**) and unique transcripts (UMIs) (**b**) per cell in each hamster snRNA-seq sample.

**c**,**d**, UMAP plots showing 43,243 nuclei across 7 hamster samples and their Leiden clustering.

**e**,**f**, UMAP plots showing an integrated dataset containing 45,553 hamster and mouse nuclei, and their separation into major cell types.

929 **g**, Dot plot showing the expression of select gene markers of each major neuronal and
930 non-neuronal cell type. Color indicates gene expression scaled across different cell types.
931 Circle size indicates the percentage of cells expressing each marker gene.

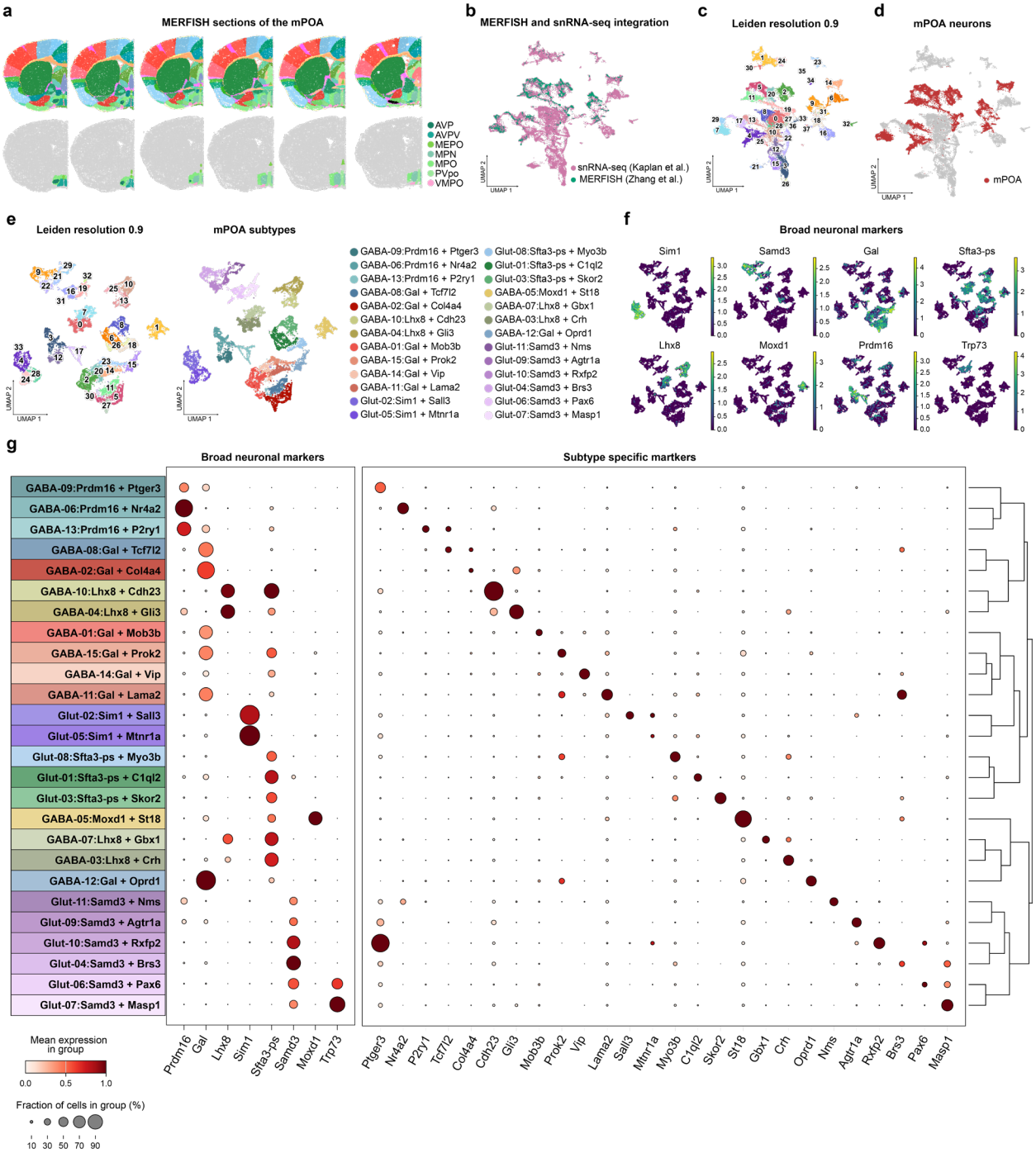


**Extended Data Fig. 4 Creation of a mouse mPOA reference transcriptomic dataset.** A mouse reference transcriptomic dataset restricted to cell types in our target regions – the medial and median POA (mPOA) – was generated. To this end, mouse spatial transcriptomic data (MERFISH)[61] was subset to only include neurons found in the mPOA

937 and co-clustered with mouse neuronal snRNA-seq populations from Extended Data Fig.
938 3f, g, enabling the annotation of 15 GABAergic and 11 glutamatergic mPOA neuronal
939 populations in the mouse snRNA-seq dataset.
940 **a**, Coronal brain sections indicating subregions of the mPOA. MERFISH data was subset
941 to only include neurons within the indicated mPOA regions.
942 **b**, UMAP plot showing the integrated MERFISH mPOA and mouse snRNA-seq dataset.
943 **c**,**d**, UMAP plot showing Leiden clustering (**c**) and regional annotation (**d**) of the integrated
944 MERFISH mPOA and mouse snRNA-seq dataset.
945 **e**, UMAP plot of only mPOA neurons from (d) colored by Leiden cluster number (left), or
946 annotated clusters (right). Annotation comprises cell class (Glut = glutamatergic, GABA
947 = GABAergic), followed by key marker genes. These cells comprise the mouse mPOA
948 reference transcriptomic dataset.
949 **f**, UMAP plot showing expression of select marker genes in mouse mPOA.
950 **g**, Dot plot showing the expression of cell-type-specific marker genes in mouse mPOA.

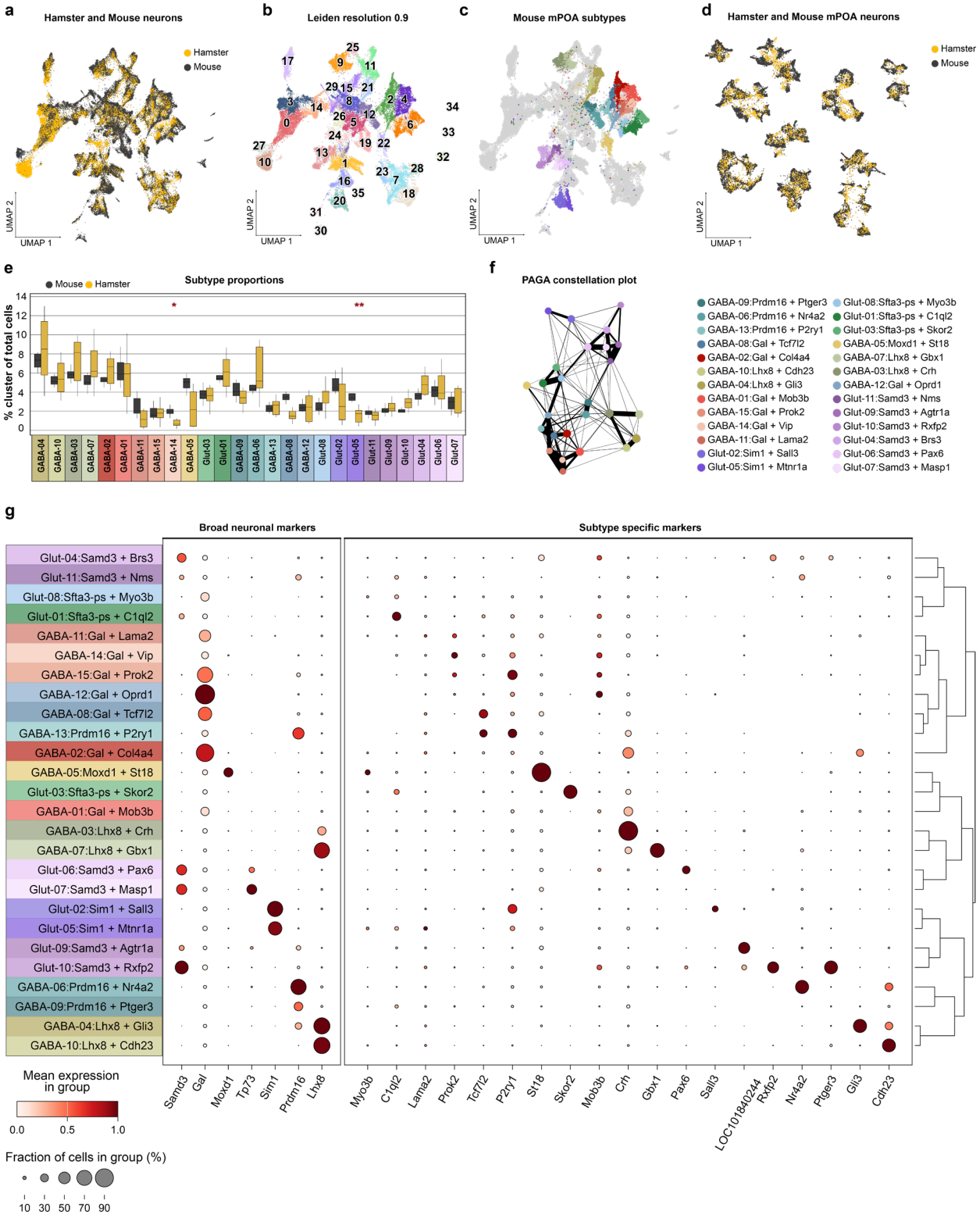


**Extended Data Fig. 5 Integration of hamster snRNA-seq with the mouse mPOA reference transcriptomic dataset.**

954 Leveraging the annotations from the mouse mPOA reference transcriptomic dataset
955 (Extended Data Fig. 4), we annotated neurons from the hamster POA snRNA-seq dataset
956 to generate the final cross-species atlas.
957 **a**,**b**, UMAP plot showing integrated hamster and mouse neuronal snRNA-seq data,
958 colored by species of origin (**a**), or Leiden cluster (**b**).
959 **c**, UMAP plot highlighting the location of mouse mPOA neurons, colored based on
960 clusters from the mouse mPOA reference transcriptomic dataset.
961 **d**, UMAP plot as in Fig. 3 displaying all mouse and hamster mPOA neurons from the
962 snRNA-seq dataset, colored by the clusters defined in the mouse mPOA reference
963 transcriptomic dataset.
964 **e**, Relative abundance of each cell type in the mouse and hamster POA dataset. Three
965 cell types show significant differences in abundance (* $P < 0.05$, ** $P < 0.01$, Mann-
966 Whitney U test).
967 **f**, Constellation plot showing the relationships between subtypes based on their latent
968 space.
969 **g**, Dot plot showing the expression of cell-type-specific marker genes for hamster
970 neurons.

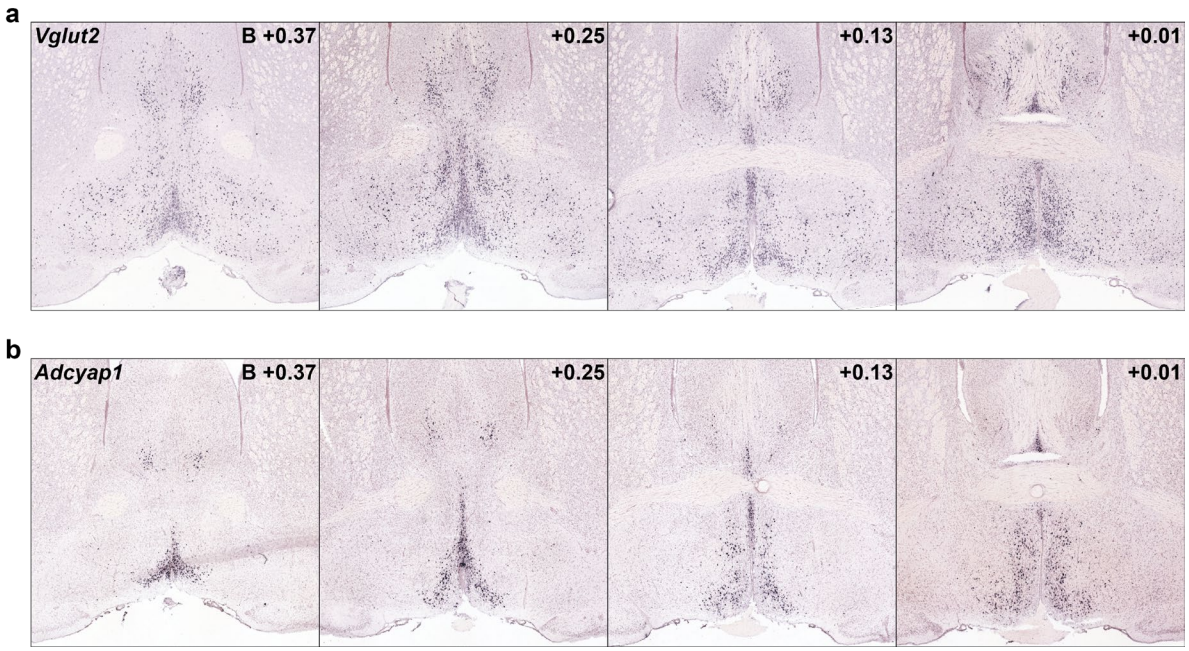


**Extended Data Fig. 6 Anatomical distribution of mouse FIT-associated neurons.** **a**,**b**, Example coronal sections of the mouse brain containing the anterior POA, showing ISH signal for marker genes *Slc17a6/Vglut2* (**a**) and *Adycap1* (**b**). Data from mouse.brain-map.org[85].

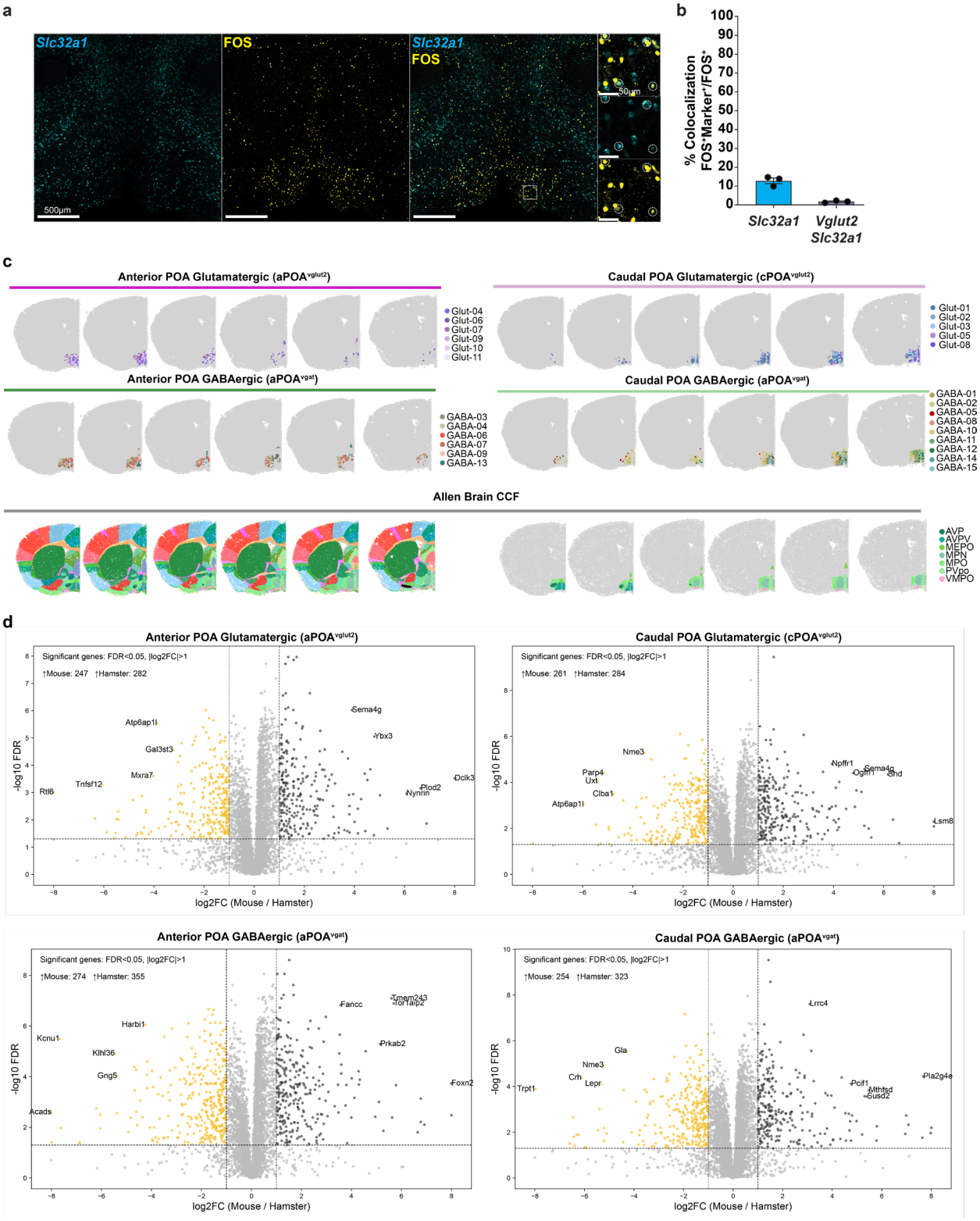
a
Slc32a1
FOS
Slc32a1
FOS
500μm
50μm
b
% Colocalization
FOS+Marker+/FOS+
Slc32a1
Vglut2
Slc32a1
c
Anterior POA Glutamatergic (aPOAvglut2)
Glut-04
Glut-06
Glut-07
Glut-09
Glut-10
Glut-11
Caudal POA Glutamatergic (cPOAvglut2)
Glut-01
Glut-02
Glut-03
Glut-05
Glut-08
Anterior POA GABAergic (aPOAvgat)
GABA-03
GABA-04
GABA-06
GABA-07
GABA-09
GABA-13
Caudal POA GABAergic (aPOAvgat)
GABA-01
GABA-02
GABA-05
GABA-08
GABA-10
GABA-11
GABA-12
GABA-14
GABA-15
Allen Brain CCF
AVP
AVPV
MEPO
MPN
MPO
PVpo
VMPO
d
Anterior POA Glutamatergic (aPOAvglut2)
Significant genes: FDR<0.05, |log2FC|>1
↑Mouse: 247 ↑Hamster: 282
Sema4g
Ybx3
Atp6ap1l
Gal3st3
Mxra7
Tnfsf12
Rtl6
Plod2
Nynrin
Dclk3
-log10 FDR
log2FC (Mouse / Hamster)
Caudal POA Glutamatergic (cPOAvglut2)
Significant genes: FDR<0.05, |log2FC|>1
↑Mouse: 261 ↑Hamster: 284
Nme3
Parp4
Uxt
Clba1
Atp6ap1l
Npffr1
Ogfrl1
Sema4g
Snd
Lsm8
-log10 FDR
log2FC (Mouse / Hamster)
Anterior POA GABAergic (aPOAvgat)
Significant genes: FDR<0.05, |log2FC|>1
↑Mouse: 274 ↑Hamster: 355
Fancc
Tmem243
Tor1aip2
Harbi1
Kcnu1
Klhl36
Gng5
Prkab2
Foxn2
Acads
-log10 FDR
log2FC (Mouse / Hamster)
Caudal POA GABAergic (aPOAvgat)
Significant genes: FDR<0.05, |log2FC|>1
↑Mouse: 254 ↑Hamster: 323
Lrrc4
Gla
Nme3
Crh
Lepr
Trpt1
Pcif1
Mthfsd
Cusd2
Pla2g4e
-log10 FDR
log2FC (Mouse / Hamster)

976

977 **Extended Data Fig. 7 Marker expression of DT-active neurons; anatomical**
978 **localization and cross-species differential gene expression of POA neuronal**
979 **populations.**

980 **a**, Example coronal sections showing the aPOA of a Syrian hamster collected during DT
981 onset. Immunofluorescent staining against FOS indicates the location of active neurons
982 (yellow), whereas ISH indicates the expression of the marker gene *Slc32a1* (*Vgat*). High-
983 magnification images are shown as insets with example FOS+ *Slc32a1*+ cells circled.

984 **b**, Quantification of the fraction of FOS+ neurons during torpor that express *Slc32a1*
985 (12.8% ± 1.5, animals = 3) and dual-expressing *Slc17a6/Slc32a1* (1.8% ± 0.3, n = 3)
986 neurons. Data presented as mean ± s.e.m.

987 **c**, MERFISH plot showing the spatial distribution of neuronal subtypes in the mouse POA
988 separated by their major cell types and anatomical location.

989 **d**, Differential gene expression between hamster and mouse neurons across the four
990 major neuron groups.

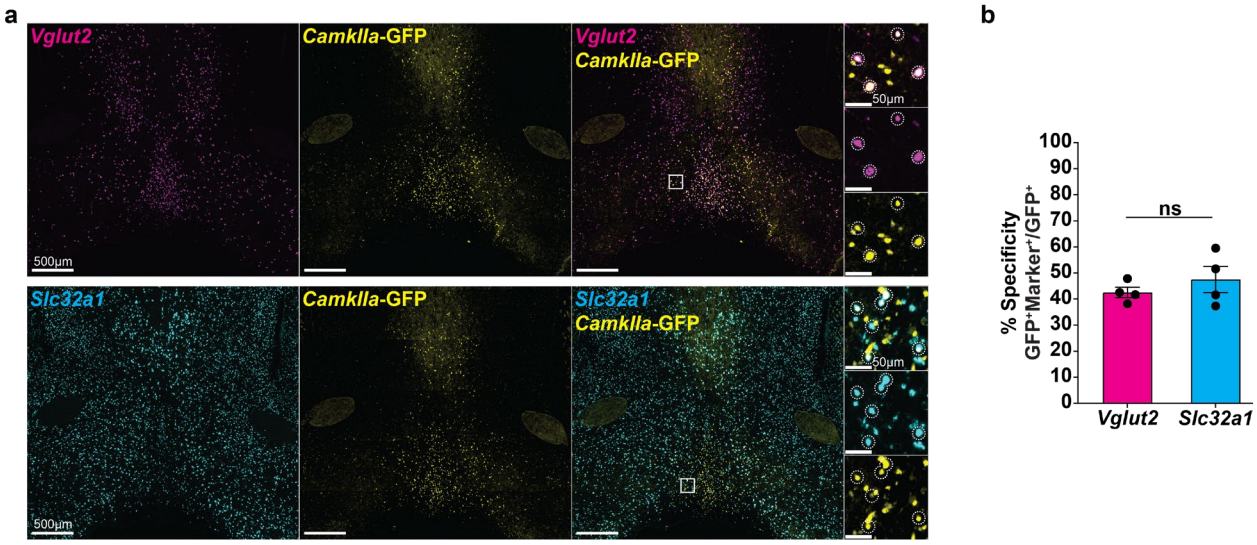


**Extended Data Fig. 8 *CamkIIa* promoter-based AAVs lack specificity for glutamatergic neurons in the hamster aPOA.**

Hamsters (n = 4) were stereotaxically administered AAV8-CamkIIa-GFP and harvested ~2 weeks later for immunostaining and ISH.

**a**, Example coronal sections showing the hamster POA comprising AVPe, MPA, and MnPO. Immunofluorescent staining against GFP indicates the location of virally labeled cells (yellow), whereas ISH indicates the expression of genes *Slc17a6* (*Vglut2; magenta*) and *Slc32a1 (Vgat; cyan)*. High-magnification images are shown on the right with example GFP+ *Marker+* cells circled.

**b**, Quantification of the fraction of AAV-CamkIIa-GFP+ neurons that express *Slc17a6* (42.6% ± 2.0, animals = 4), and *Slc32a1* (47.5 ± 5.0%, animals = 4). Data presented as mean ± s.e.m.

a

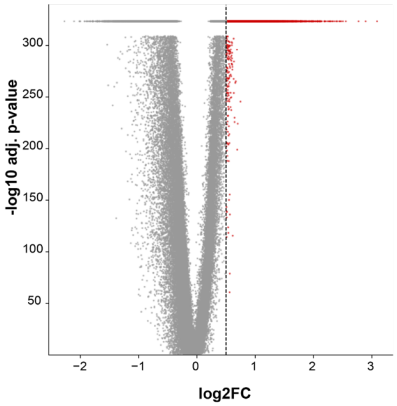


b

| | Genomic coordinates (mm10) | Nearest gene |
|---|---|---|
| GRE 1 | chr10:26228096-26228596 | Samd3 |
| GRE 2 | chr19:59457295-59457795 | Emx2 |
| GRE 3 | chr6:111965822-111966322 | Gm26362 |
| GRE 4 | chr10:41139206-41139706 | Gm32338 |
| GRE 5 | chr11:91056877-91057377 | 4930405D11Rik |
| GRE 6 | chr13:69317802-69318302 | Gm4812 |
| GRE 7 | chr16:96450604-96451104 | Gm32358 |
| GRE 8 | chr16:23505809-23506309 | Gm49514 |
| GRE 9 | chr19:23085045-23085545 | C330002G04Rik |
| GRE 10 | chr16:63743408-63743908 | Gm22769 |
| GRE 11 | chr11:109106715-109107215 | E030025P04Rik |
| GRE 12 | chr13:75113945-75114445 | Pcsk1 |

c

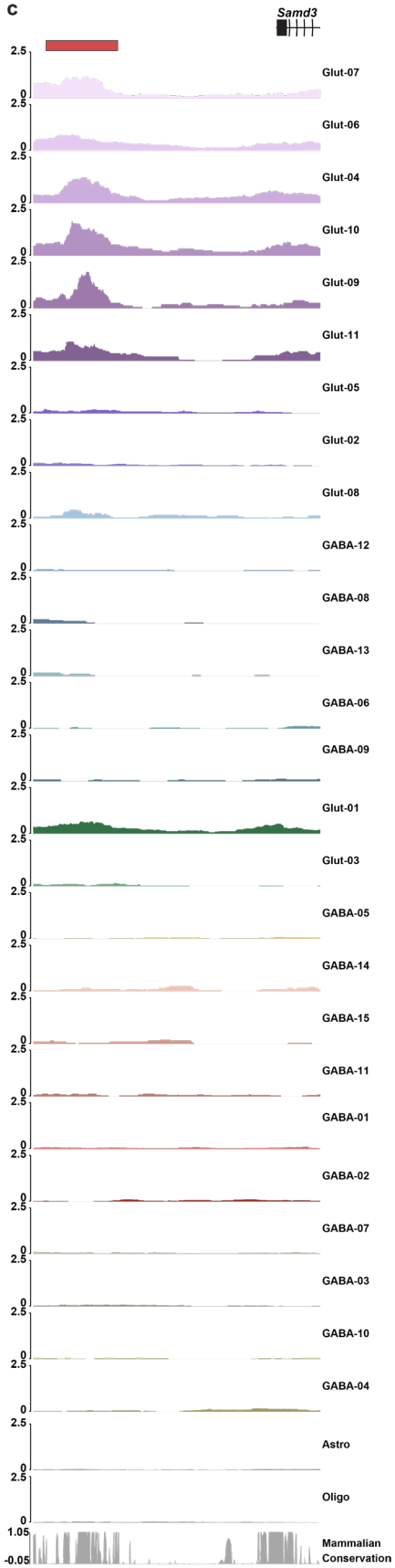


d

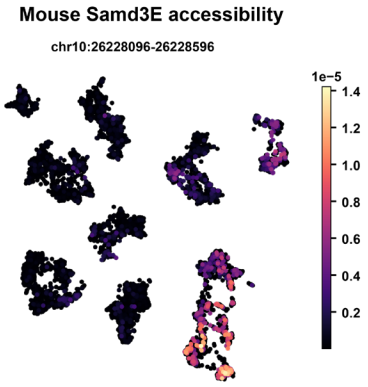


e

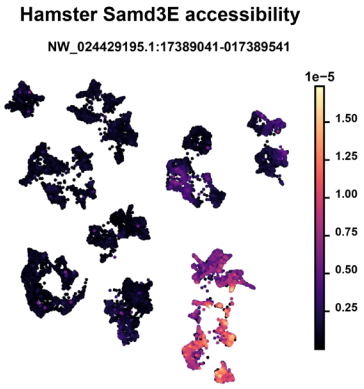


1004

1005 **Extended Data Fig. 9 snATAC-seq analysis reveals *Samd3E* as tool to target POA**
1006 **neurons.**

1007 **a**, Differential accessibility analyses of genomic elements in aPOA$^{Vglut2}$ neurons vs. all
1008 other neurons in mice; top regions (log2FC > 0.5) are marked in red for further analysis.

1009 **b**, Genomic location and nearest gene of the top candidate putative GREs.

1010 **c**, ATAC-seq genome browser tracks (normalized counts per location) of individual mouse
1011 neuronal subtypes showing the mouse *Samd3*-proximal putative GRE (*Samd3E,* red
1012 box), with accompanying sequence conservation below.

1013 **d**,**e**, UMAP feature plots depicting *Samd3E* accessibility in the indicated species.

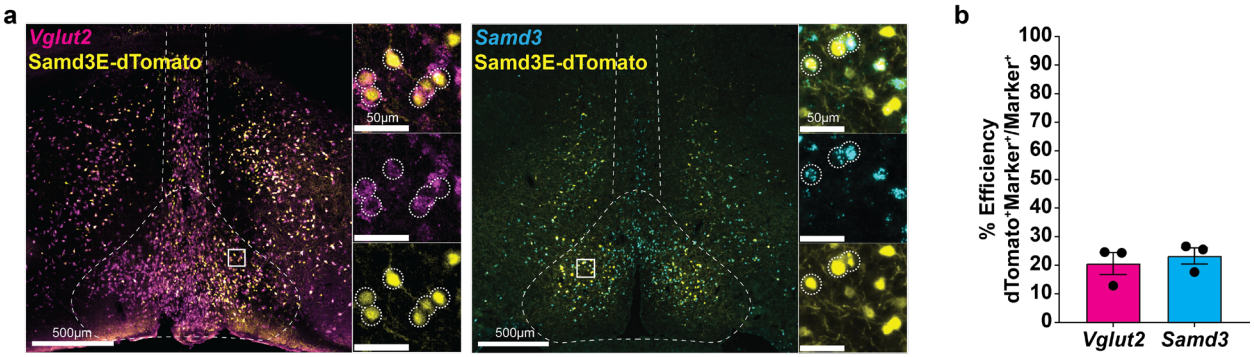


**Extended Data Fig. 10 Samd3E-AAV transduction efficiency.**

**a**, Efficiency of targeting aPOA$^{Vglut2}$ and aPOA$^{Samd3}$ neurons with AAV8-Samd3E-dTomato. Syrian hamsters (n = 3) were injected with AAV8-Samd3E-dTomato. Immunofluorescent staining against dTomato was used to identify virally labeled cells (yellow), whereas ISH indicates the expression of the marker gene *Slc17a6* (*Vglut2*, magenta) and *Samd3* (cyan), as in Fig. 4g.

**b**, Quantification of the fraction of *Slc17a6*+ cells that also express dTomato+ (20.6 ± 3.9%, animals = 3) and *Samd3*+ cells that also express dTomato+ (23.3 ± 2.8%, animals = 3). Given limited viral spread, this quantification was limited to the area of viral expression within the aPOA. These results indicate that AAV8-Samd3E-dTomato achieves high specificity and modest efficiency for targeting aPOA$^{Vglut2}$ and aPOA$^{Samd3}$ neurons.

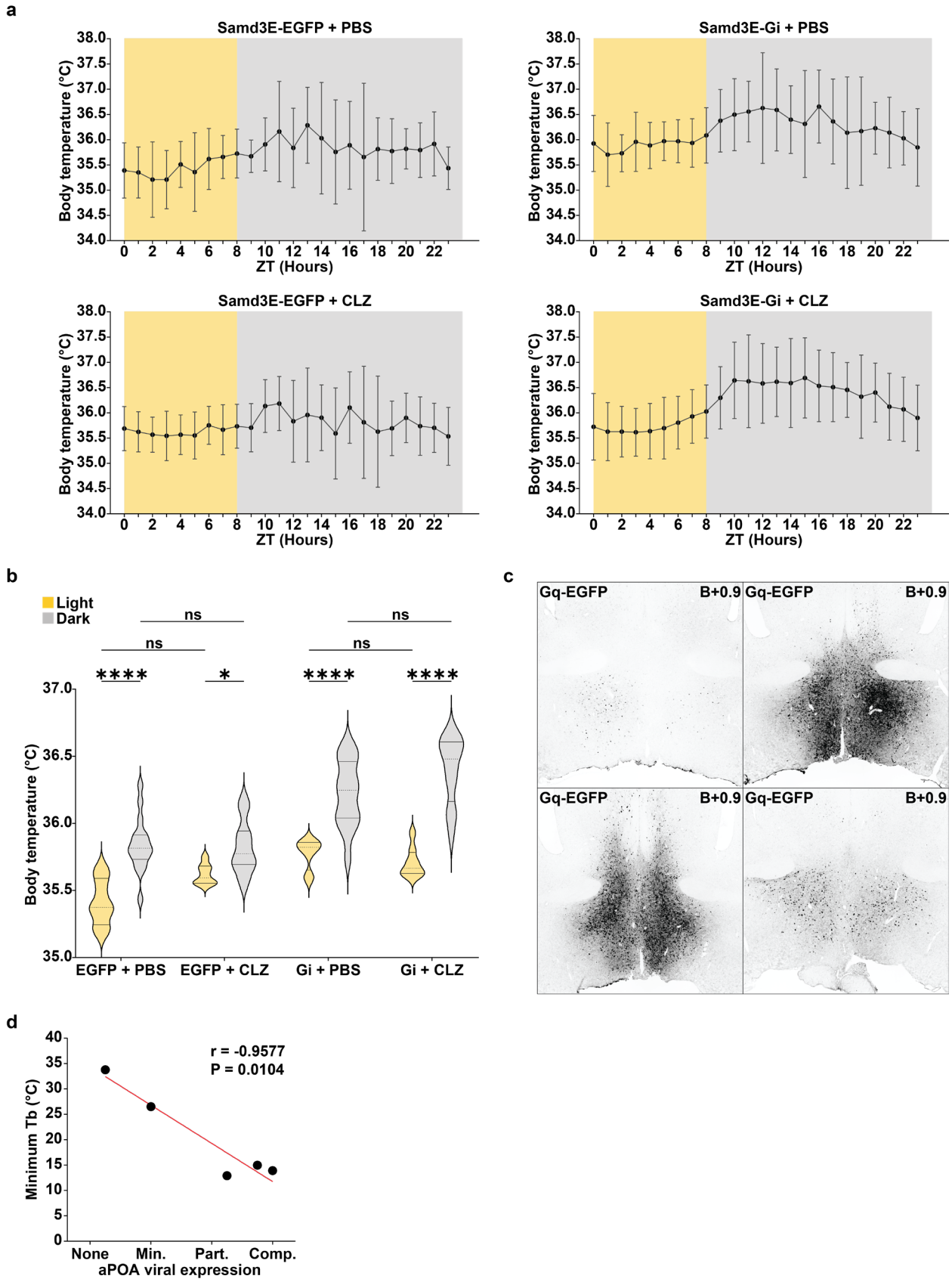
a
Samd3E-EGFP + PBS
Samd3E-Gi + PBS
Samd3E-EGFP + CLZ
Samd3E-Gi + CLZ
Body temperature (°C)
ZT (Hours)
b
Light
Dark
ns
****
*
Body temperature (°C)
EGFP + PBS
EGFP + CLZ
Gi + PBS
Gi + CLZ
c
Gq-EGFP
B+0.9
d
r = -0.9577
P = 0.0104
Minimum Tb (°C)
None
Min.
Part.
Comp.
aPOA viral expression

1027

1028 **Extended Data Fig. 11 Circadian $T_b$ patterns and correlation between viral aPOA**
1029 **expression and $T_b$ decrease.**

1030 **a**, Circadian fluctuation of $T_b$ in Samd3E-EGFP- and Samd3E-Gi-DREADD-injected
1031 hamsters following administration of CLZ (5 mg/kg) or control PBS. Light and dark cycle
1032 phases are represented by yellow and grey, respectively. Data presented as mean ± s.d.
1033 of core body temperatures during each hour.

1034 **b**, Violin plot quantification of body temperature range between light (yellow) and dark
1035 (grey) phases of Samd3E-EGFP- (n = 5 animals) or Samd3E-Gi-DREADD-injected
1036 animals (n = 12) following CLZ or control PBS administration (Tukey's multiple
1037 comparisons test; *P-adjusted < 0.05, ****P-adjusted < 0.0001, ns = not significant P >
1038 0.05).

1039 **c**, Immunofluorescence images in the aPOA of additional Samd3E-Gq-DREADD-EGFP-
1040 injected animals.

1041 **d**, Correlation between minimum $T_b$ reached following CLZ administration and viral
1042 expression within the aPOA (n = 5 animals, r = -0.95, P = 0.01).

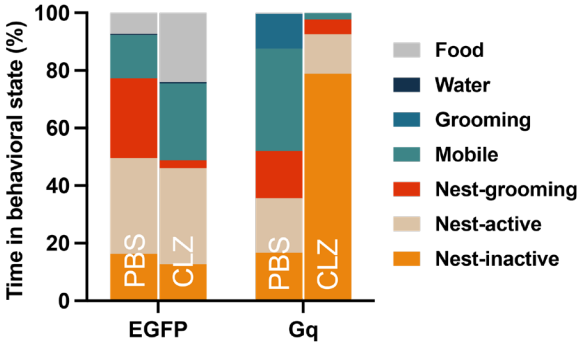


1043

1044 **Extended Data Fig. 12 Changes in behavioral repertoire after aPOA$^{Vglut2}$ neuronal**

1045 **activation.**

1046 Percentage of time in behavioral states over a 10 min observation window post-injection

1047 with PBS or CLZ across all hamsters injected with AAV-Samd3E-EGFP-P2A-

1048 Synaptophysin-mRuby (n = 3) and AAV-Samd3E-hM3D(Gq)-nlsGFP (n=6).

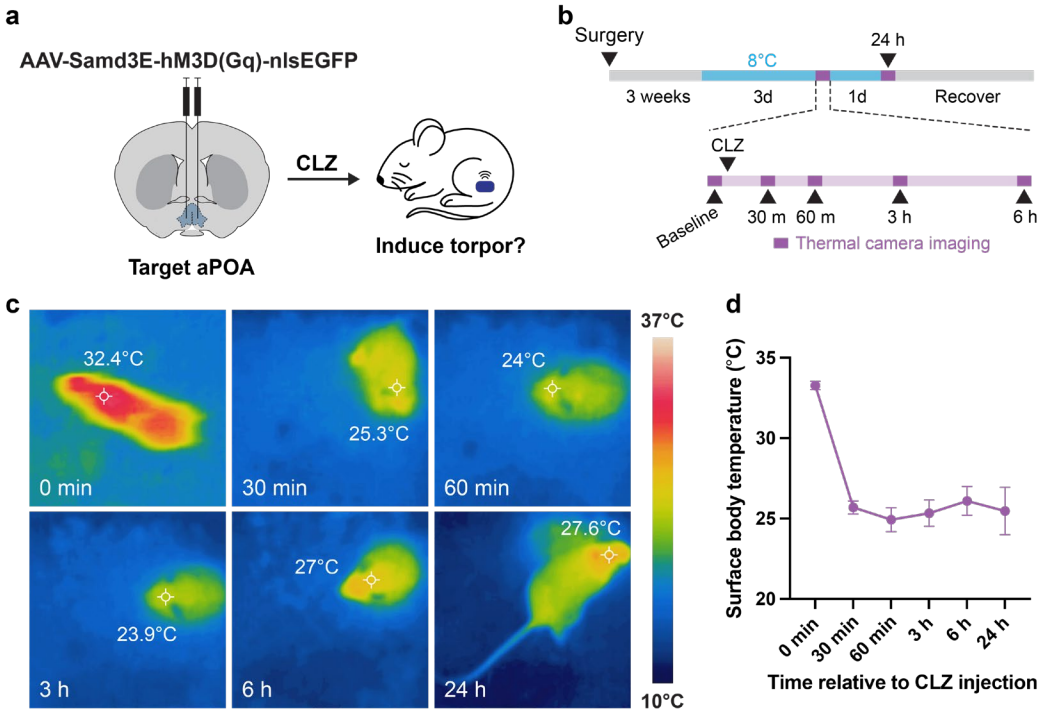


**Extended Data Fig. 13 Stimulation of aPOA$^{Vglut2}$ neurons in mice and resulting body temperature change.**

**a**, Schematic of experimental design.

**b**, Timeline of experiment and analysis. Mice were acclimated to 8°C for 3 days before injection with CLZ (5 mg/kg) and imaged with a thermal camera at baseline, 30 min, 60 min, 3 hours, 6 hours, and 24 hours post injection at 8°C.

**c**, Representative thermographic images obtained by chemogenetic stimulation of aPOA$^{Vglut2}$ neurons.

**d**, Surface body temperature before (0 min) and after (30 min to 24 h) CLZ injection (n=7 mice). Data are presented as mean ± s.e.m.

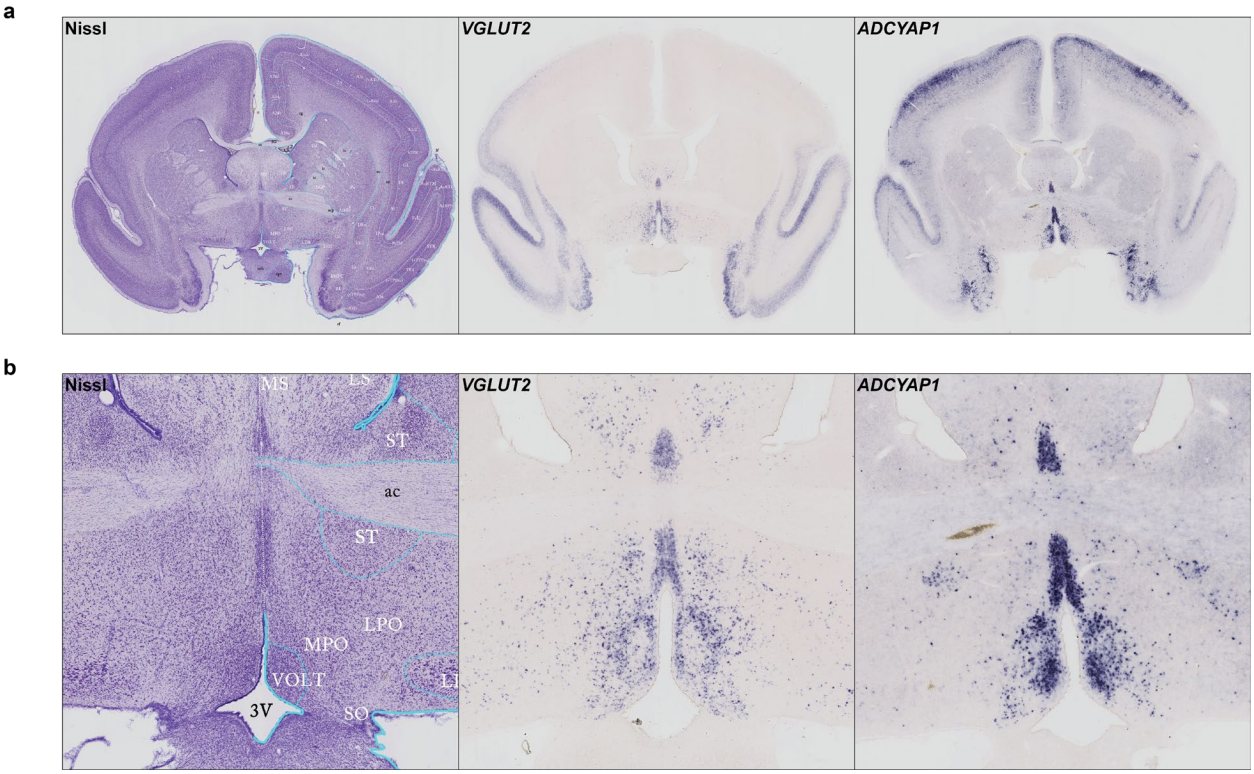


**Extended Data Fig. 14 *In situ* hybridization for marker of torpor-associated genes in marmosets.**

**a**, Example coronal sections of the marmoset brain containing the anterior POA showing ISH signal for marker genes *Slc17a6/Vglut2* and *Adycap1*.

**b**, Higher resolution images from (a) displaying the anterior POA. Data from https://gene-atlas.brainminds.jp/[72–74].